

# Design criteria for pin-ended hot-rolled and laser-welded stainless steel equal-leg angle columns

Jelena Dobrić<sup>a,\*</sup>, Aljoša Filipović<sup>a</sup>, Nancy Baddoo<sup>b</sup>, Dragan Buđevac<sup>a</sup>, Barbara Rossi<sup>c</sup>

<sup>a</sup> University of Belgrade, Faculty of Civil Engineering, Serbia

<sup>b</sup> Steel Construction Institute, United Kingdom

<sup>c</sup> University of Oxford, Department of Engineering Science

\* Corresponding author: [jelena@imk.grf.bg.ac.rs](mailto:jelena@imk.grf.bg.ac.rs)

## Highlights:

1. Structural response of pin-ended hot-rolled and laser-welded stainless steel angle columns studied.
2. FE parametric studies including geometric and material nonlinearity carried out.
3. Accuracy of European and North American codified procedures assessed.
4. Proposal provided for European buckling curves.
5. Reliability analysis of proposed design criteria performed.

# Design criteria for pin-ended hot-rolled and laser-welded stainless steel equal-leg angle columns

## Abstract

This paper explores an attempt to investigate the structural behaviour and design of equal-leg stainless steel angle columns fabricated by the laser-welding of individual hot-rolled plates and by hot-rolling process. The studies cover columns with pin-ended boundary conditions exposed to pure axial compression. An advanced and realistic finite element model able to replicate the buckling features of stainless steel angle columns is developed and validated against available experiments collected in the literature. Employing the validated finite element model, quantitative numerical parametric studies, considering minor-axis flexural buckling, as well as flexural-torsional buckling, are performed. Based on comprehensive benchmark data, the accuracy, safety and applicability of the existing column design procedures provided in the European and North American structural stainless steel codes are assessed. The evaluation results reveal that the North American codified design procedures lead to conservative and scattered resistance predictions, thereby demonstrating a need for their improvement. As a result of conducted studies, the new criteria for design of pin-ended hot-rolled and laser-welded stainless steel equal-leg angle columns are proposed. Their suitability for inclusion in the European structural stainless steel design code is confirmed by statistical reliability analyses in accordance with EN 1990.

**Key-words:** Hot-rolled stainless steel angle section; Laser-welded stainless steel angle section; Flexural-torsional buckling; Flexural buckling; Finite Element Modelling; Design.

## 1. Introduction

The structural responses of stainless steel equal-leg angle section columns fabricated by hot-rolling, arc-welding or high-precision laser-welding techniques, buckling in flexural buckling (FB) or flexural-torsional buckling (FTB) modes, are not explicitly addressed in the current European code for stainless steel structures EN 1993-1-4 [1]. Consequently, to fill the gap created by the lack of experimental data and the scarcity of research information, several scientific projects, aiming to examine the buckling features of hot-rolled stainless steel (HRSS) and laser-welded stainless steel (LWSS) angle columns, have been undertaken over the last few years.

De Menezes et al. [2] performed 13 tests on fixed-end HRSS equal-leg angle columns produced from austenitic grade to study their global buckling responses. Based on performed experiments, the authors conducted finite element (FE) parametric studies aiming to evaluate the design procedure prescribed in EN 1993-1-4 [1]. As a result, a revised Eurocode 3 buckling curve involving the better-suited values for the imperfection factor  $\alpha = 0.6$  and the limiting slenderness  $\bar{\lambda}_0 = 0.23$  was proposed to predict column minor-axis FB resistance. Liang et al. [3] carried out tests on 16 fixed-end austenitic HRSS equal-leg angle section columns complemented by numerical analyses. Concerning column FTB responses, the authors demonstrated that the current codified design procedures [1], [4], [5] give conservative and scattered column resistance predictions, whereas the novel Direct Strength Method (DSM)-based design method [6], originally developed for cold-formed carbon steel angle columns, offers a substantially improved level of design accuracy but sometimes may result in noticeable unsafe errors. A similar outcome related to DSM was found in the case of other nonlinear materials; Wang et al. [7] carried out an investigation into the behaviour of fixed-ended high-strength aluminium alloy angle-section columns. It was found that the existing codes for design of aluminium alloy structures [8],[9], [10] yield accurate predictions for FB while providing unduly conservative and scattered predictions for FTB column failures. On the other hand, the new DSM-based design approach [6], [11] sufficiently captures the column FTB behaviour with a reasonable amount of accuracy. To investigate the cross-section behaviour and compressive capacities, Sun et al. [12] performed stub column tests on HRSS angles produced from different austenitic grades. Sirqueira et al. [13] and Sarquis et al. [14] reported a series of FTB tests on fixed-ended austenitic HRSS equal-leg angle columns. Sarquis et al. [14] also carried out

complementary numerical analyses to underpin the development of the new procedures for column FTB resistances based on Eurocode 3 design approach. Zhang et al. [15] performed an experimental and numerical modelling programme to investigate minor-axis FB behaviour of HRSS equal-leg angle columns. Based on gained results, the authors demonstrated applicability of Eurocode 3 [1] and the AISC 27 [16] design procedures and evidenced that a revised Eurocode 3 design curve, proposed in the fourth edition of the Design Manual for Structural Stainless Steel [17], with an imperfection factor  $\alpha = 0.76$  and limiting slenderness  $\bar{\lambda}_0 = 0.20$  can predict minor-axis FB strengths of pin-ended HRSS angle columns with reasonable and safe-sided accuracy. Filipović et al. [18], [19] performed a comprehensive and systematic experimental programme on pin-ended HRSS and LWSS equal-leg angle columns to examine different buckling modes affected by column slenderness and initial structural imperfections caused by different fabrication processes. It was shown that the ultimate strengths of tested HRSS angle columns are higher than those obtained in the case of LWSS angle columns with the same nominal geometries, for both stub-column tests and global buckling tests.

This paper presents a comprehensive and advanced numerical modelling programme concerning the pin-ended HRSS and LWSS equal-leg angle columns under pure axial compression aiming to highlight the main differences between the column buckling responses and provide database for design criteria development. FE models, able to replicate the key experimental results—load vs. lateral deflections, load vs. axial strain and the observed failure buckling modes, are developed and validated against experiments performed by Filipović et al. [18], [19]. Upon validation of the FE models, parametric studies are conducted covering columns with a significant range of cross-section dimensions and steel grades available on the market — a majority of the HRSS and LWSS equal-leg angle profiles are fabricated from common austenitic grades with maximum leg length of 150 mm for hot-rolled angles and maximum leg length of 300 mm for laser-welded angles [20]. The codified procedures in EN 1993-1-4 [1], EN 1993-1-1 [21] and AISC 27 [16], AISC 360 [22], are evaluated through comparisons between experimental data collected from literature and numerical data on the one side, and equivalent design data on the other side. The appropriateness of mentioned design approaches is assessed through (i) the quality of the estimation of the available failure load data, and (ii) the evaluation of the corresponding partial safety factor  $\gamma_{M1}$  for column resistance.

## 2. FE modelling and validation

This section provides the details of the FE modelling approach adopted in the study and its validation against experimental results from the literature. The advanced and realistic numerical simulations of the experiments carried out on HRSS equal-leg angle columns [18] and LWSS equal-leg angle columns [19] were performed using the FE code ABAQUS [23]. Numerical simulations were performed for all tests: stub column tests on short length specimens, FTB and minor-axis FB tests on intermediate length and large length specimens, respectively. The columns were divided into test series depending on their cross-section dimensions and nominal lengths, as it is reported in Table 1. The specimen designations given herein are in accordance with experiments [18], [19]: Angle Hot Rolled (AHR), Angle Laser Welded (ALW), leg width  $b \times$  leg width  $b \times$  leg thickness  $t$  – column length  $L$ .

**Table 1.** Nominal geometrical dimensions of the specimens in experiments [18], [19].

Manufacture process	Specimen designation	Length $L$ (mm)	Width of leg $b$ (mm)	Thickness $t$ (mm)	Radius at corner $r_1$ (mm)
Hot-rolling process	AHR $60 \times 60 \times 6 - 180$	180	60	6.0	7.5
	AHR $60 \times 60 \times 6 - 800$	800			
	AHR $60 \times 60 \times 6 - 2000$	2000			
	AHR $100 \times 100 \times 10 - 300$	300	100	10.0	7.0
	AHR $100 \times 100 \times 10 - 500$	500			
	AHR $100 \times 100 \times 10 - 1500$	1500			
	AHR $100 \times 100 \times 10 - 2500$	2500			
Laser-welding process	ALW $60 \times 60 \times 6 - 180$	180	60	6.0	-
	ALW $60 \times 60 \times 6 - 800$	800			
	ALW $60 \times 60 \times 6 - 2000$	2000			
	ALW $100 \times 100 \times 10 - 300$	300	100	10.0	-
	ALW $100 \times 100 \times 10 - 500$	500			
	ALW $100 \times 100 \times 10 - 1500$	1500			
	ALW $100 \times 100 \times 10 - 2500$	2500			

Two types of numerical analyses were performed for each FE model: an eigenvalue linear bifurcation analysis (LBA) and a geometrically and materially non-linear buckling analysis (GMNIA). LBA was previously employed to predict the linear bifurcation mode-shapes used to model the distributions of the initial geometric imperfections and allow for an incremental non-linear procedure. GMNIA was performed as quasi-static with the dynamic explicit solver, as it was already successfully used for simulations of column buckling tests on cold-formed stainless steel (CFSS) angle columns [24]. The mass scaling technique with a time increment of  $3 \times 10^{-6}$  s was used to shorten the computational time. Scaling was set as variable (recomputed in every integration step) and non-uniform (different for each FE) as it is the most efficient for

those models with large spectra of element sizes. An appropriate smooth curve was adopted for amplitude functions in all loading steps to avoid large inertial forces in the quasi-static analysis.

The reduced integrated eight node hexahedron solid elements C3D8R were adopted to model the nominal geometry of the tested columns. To properly account for the column bending stiffness, a global element size ranging from 2 to 3 mm was used for each FE model allowing at least three elements through the leg thickness.

The boundary conditions (BCs) of the FE models were defined in accordance with those adopted in the experiments [18], [19], where the end fixtures in the test machine for pin-ended specimens were designed to allow rotations about the minor-axis, while restraining major-axis rotations as well as twist rotations and warping. To replicate the realistic hinged supports of specimens in global buckling tests, the knife-edge assemblies (end bearing plates attached to hardened steel knife-edge device) together with top and bottom adjustable clamps that allowed the specimen alignment in the testing machine, were also modelled using the same C3D8R hexahedral solid elements. The global element size of the bearing plates was 5 mm, whereas the element size was reduced to 2 mm in the knife-edge zone to increase accuracy of the modelled geometry in the loading area. A uniform mesh with a size of 4 mm was employed to model both adjustable clamps. Contact conditions between the steel clamps and the bearing plates at the top and bottom ends of the specimen were established using tie constraints on the joining surfaces. The surface-to-surface general contact interaction procedure was chosen in the FE software package, to account for the interactions between perimeter surfaces of specimen's ends and both adjustable clamps and bearing plates. The same contact interaction was used between the top and bottom knife-edge assemblies. The "hard contact" formulation of normal behaviour and the "penalty friction" formulation of tangential behaviour were used. The friction coefficient of 0.10 was chosen for all contact surfaces, whereas between the top and bottom knife-edge assemblies the frictionless conditions were chosen, as the special treatment with lubricant grease was used in experiments to prevent friction. The calibration of the friction coefficient value was performed, finding these values as the most appropriate to match the column ultimate strengths in FE modelling and experiments. Two reference points were positioned at the centroids of the top and bottom external surfaces of the bearing plates. These reference points coincide with the longitudinal axis passing also through the centroids of the knife

edges and the modelled specimen. The top and bottom external surfaces of the bearing plates that are kinematically coupled with reference points were fixed with respect to all degrees of freedom except for the vertical displacement at the bottom loading plate where controlled nodal displacement was used to apply the compressive load [24]. In simulations of stub column tests, the end bearing plates of the testing machine were modelled as a two-dimensional rigid body. The nodal surfaces of rigid plates were kinematically constrained to the central reference points located at the centroid of the specimen end cross-sections where fixed-ended BCs were applied except for the vertical displacement at the bottom loaded edge.

The geometry and mesh of the modelled tested column, including details of the top and bottom BCs, are shown in Fig. 1.

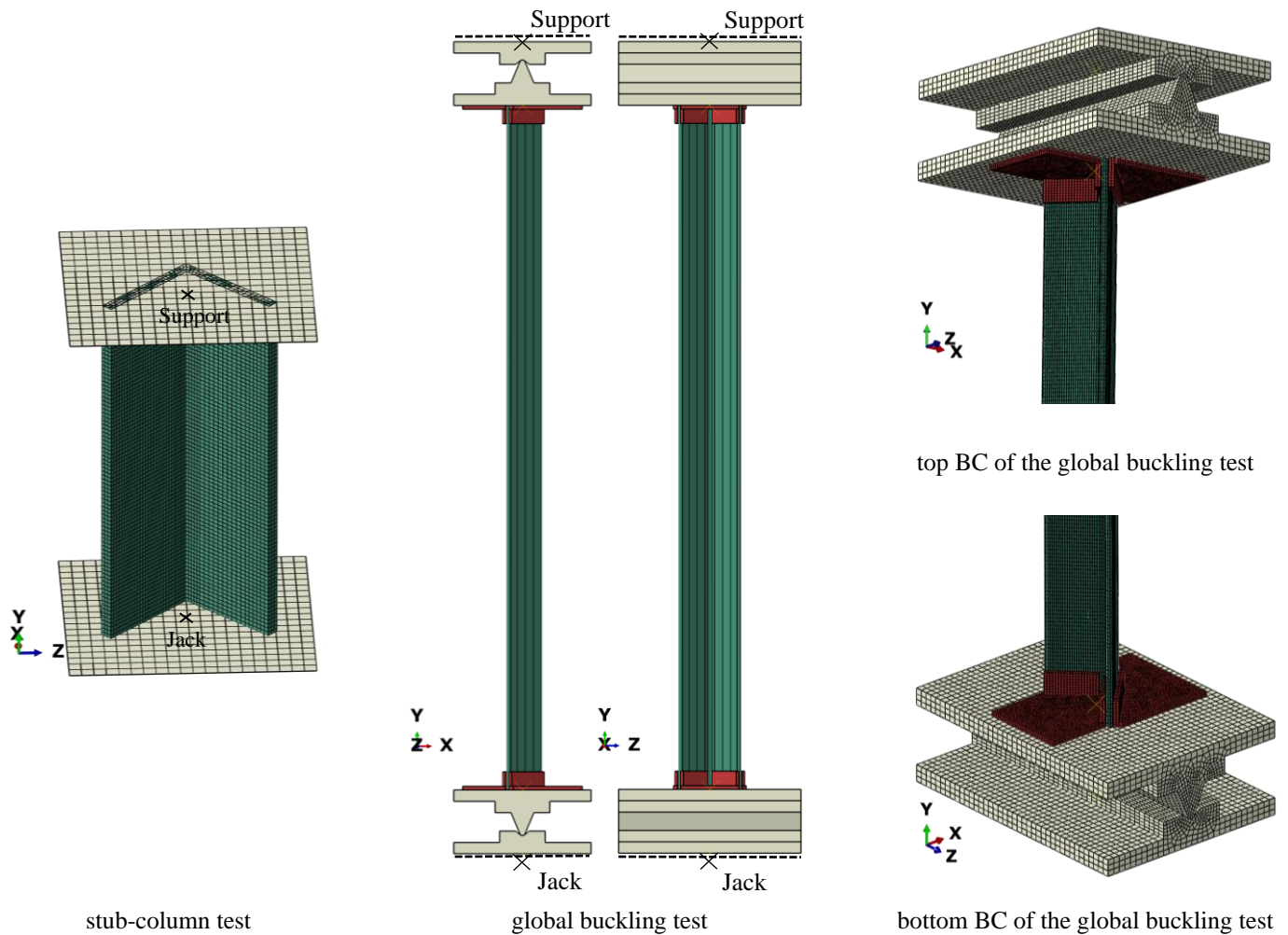


**Fig. 1** Geometry, mesh and boundary conditions of the modelled tested columns [18], [19].

In the absence of measured data, the nominal mechanical properties of steel grades S275JR and S355N were used to respectively model end adjustable clamps and the knife-edge assemblies, employing a linear elastic–perfectly plastic material model with a nominal plateau slope (these assumptions do not affect the buckling characteristics of the modelled specimens). The basic material of both tested HRSS and LWSS angle

columns was austenitic stainless steel grade EN 1.4301 (UNS S30400). To account for the material nonlinear behaviour, the measured stress–strain curves, obtained via tensile tests performed on flat coupons extracted from HRSS and LWSS angle specimens [18], [19], were incorporated into HRSS and LWSS models, respectively. Table 2 provides the material parameters included in the FE models: the yield strength  $f_y$  (taken as the 0.2 % proof strength for stainless steel grade), the ultimate tensile strength  $f_u$ , the strain corresponding to the ultimate tensile strength  $\varepsilon_u$  and the strain hardening parameters  $n$  and  $m$ .

**Table 2.** Key material properties adopted in the FE modelling.

Stainless steel or carbon steel grade / Source	$f_y$ (N/mm <sup>2</sup> )	$f_u$ (N/mm <sup>2</sup> )	$\varepsilon_u$ (%)	Strain hardening parameters	
				$n$	$m$
EN 1.4301 / Hot-rolled angles [18]	292	660	52	8	3.7
EN 1.4301 / Laser-welded angles [19]	266	637	57	9	2.9
S275JR / Steel adjustable clamps [25]	275	410	23	-	-
S355N / Steel knife-edges [26]	355	490	22	-	-

The engineering stress–strain curves used in FE material modelling are presented in Fig. 2. The Poisson’s ratio was taken as 0.3. Isotropic plasticity with isotropic strain hardening was assumed in the models using the Young’s modulus values of 200 000 and 210 000 N/mm<sup>2</sup> for stainless steel and all carbon steel grades, respectively. The engineering stress–strain responses shown in Fig. 2 were transformed into the true stress–log plastic strain and input into the ABAQUS plasticity model.

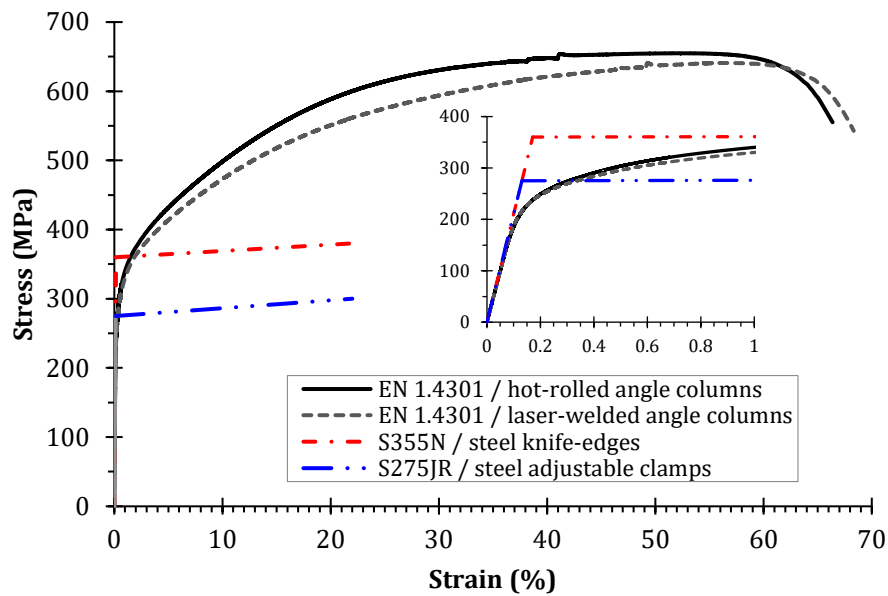


**Fig. 2** Engineering stress–strain curves adopted in the FE modelling.

The influence of residual stresses on the buckling strength of carbon steel hot-rolled equal-leg angle columns is implicitly accounted for in European specifications [27], [21] by using buckling curve  $b$  that is based on the 3-point linear predictive model of residual stress distribution. This model was developed on the basis of



relevant experimental investigations conducted in Europe in the 1970s. The distribution pattern is symmetrical with respect to the major principal axis, with compressive stresses at the legs' intersection and at their ends and equilibrating tensile stresses at the legs' mid-length. The distribution of residual stresses is uniform throughout the legs' thickness with the dominant longitudinal stress component. The 3-point distribution model was also adopted in research on buckling design criteria of carbon steel hot-rolled equal-leg angle columns performed by Kitipornchai and Lee [28] and Camotim et al. [29].

The 3-point linear model, based on measurements made on HRSS and LWSS equal-leg angle columns performed by Filipović et al. [18], [19] and shown in Fig. 3a, was used to define distributions and magnitudes of residual stresses in the FE models in this paper. As can be seen in Fig. 3a, the maximum tensile residual stresses at legs' mid-length and minimum compressive residual stress at legs' intersection are taken as  $0.42 \cdot f_y = 0.42 \cdot 290 = 122 \text{ MPa}$  and  $0.45 \cdot f_y = 0.45 \cdot 264 = 119 \text{ MPa}$  for HRSS and LWSS equal-leg angle columns, respectively. These values correspond to measured magnitudes of residual stresses found in experiments [18], [19]. Note that these magnitudes are higher in comparison with those found in the case of carbon steel angles [30], [31]. The residual stress patterns displayed in Fig. 3a and Fig. 3b were generated in the FE models through thermal simulations by means of equivalent temperature strains, as a predefined temperature field by ensuring that BCs maintain the developed equilibrium stresses in the FE model. The residual stresses were developed in an initial separate state of GMNIA that was finalised with the achievement of the equilibrium stresses prior to the application of the compressive failure load. Fig. 3c and Fig. 3d confirm that residual stresses were successfully generated into both hot-rolled and laser-welded FE models.

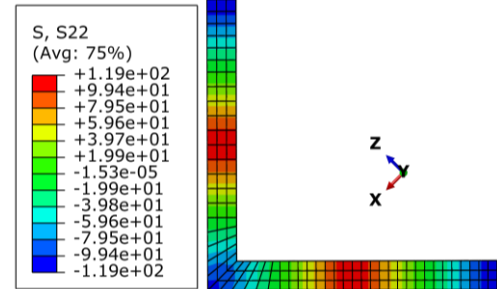
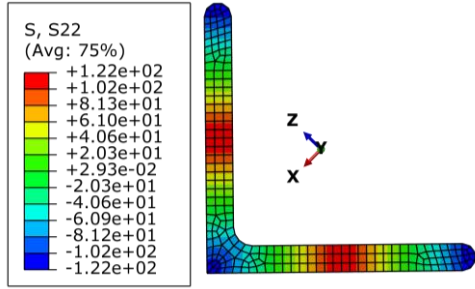
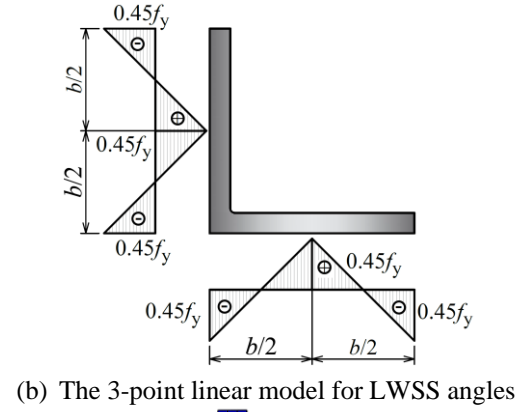
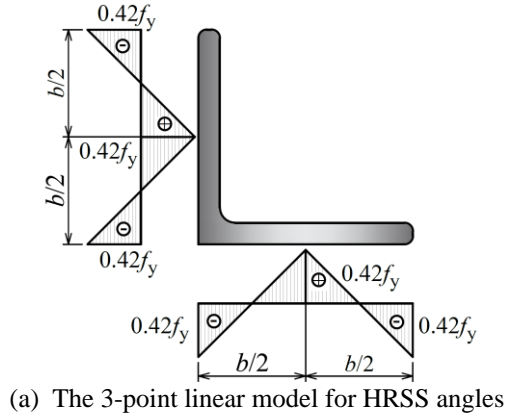


**Fig. 3** Residual stress patterns for HRSS and LWSS equal-leg angles adopted in the FE modelling.

The initial geometric imperfections were explicitly modelled by using lowest flexural-torsional and global buckling modes obtained via LBA performed on equivalent FE models with the same mesh. Two essential forms of geometric imperfections were considered: a bow imperfection about the minor-principal axis—flexural global mode, and a major-axis flexural-torsional mode (see results of imperfection sensitivity study presented in Section 3). The imperfection amplitudes were equal to the measured ones.

Upon detailed analysis of the buckling features and compressive capacities of both hot-rolled and laser-welded tested columns [18], [19], it was observed that an initial loading eccentricity about the minor-principal axis caused by adjustment errors of long specimens, was introduced in global buckling tests. Based on the readings from the linear variable displacement transducers (LVDTs) and strain gauges (SGs), the initial loading eccentricity  $e_0$  was determined as the difference between the overall loading eccentricity, obtained in accordance with recommendations given by Huang and Young [32], and the initial mid-height global geometric imperfection amplitude about the minor-principal axis. It was found that initial eccentricities  $e_0$  with values in the range from  $-1.3$  to  $1.1$  mm toward to the leg tips or the heel of the equal-leg angle section along the major-axis direction relative to the section centroid, were introduced in all repeated global buckling tests (see Fig. 4). The realistic FE modelling allowed for a sophisticated analysis of

the structural behaviour influenced by the initial eccentricity and direct comparison with the experimental results.

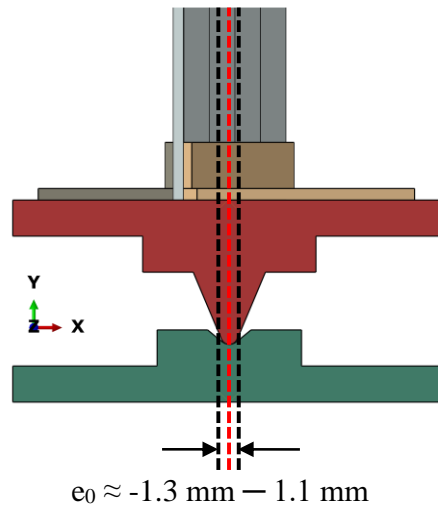


**Fig. 4** Initial end eccentricity introduced in simulations of long column tests [18], [19].

The accuracy of the FE modelling developed in this study was validated using prior experimental data [18], [19]. The comparison between the key experimental and numerical results—failure modes, ultimate buckling loads, load–strain and load–deflection curves—demonstrates that the FE models are capable of accurately estimating the structural buckling responses of both hot-rolled and laser-welded equal-leg angle specimens. The qualitative comparisons between the buckling modes observed in the FE models with those found in the stub column tests and global buckling tests are shown in Fig. 5 and Fig. 6 for selected specimens, respectively. It can be seen from the figures that the buckling patterns observed in the experiments [18], [19] are very well reproduced by the FE modelling, including inelastic FTB in stub column tests, minor-axis FB coupled with FTB and minor-axis FB in global buckling tests. Besides, distributions of axial stresses along the length of columns—which is clearly demonstrated in Fig. 6—are in a very good agreement with stress distributions found in experiments [18], [19]. Note that the FTB deformations occurring in very short length equal-leg angle columns (stub column test simulations) are predominantly torsional and very similar to local deformations.

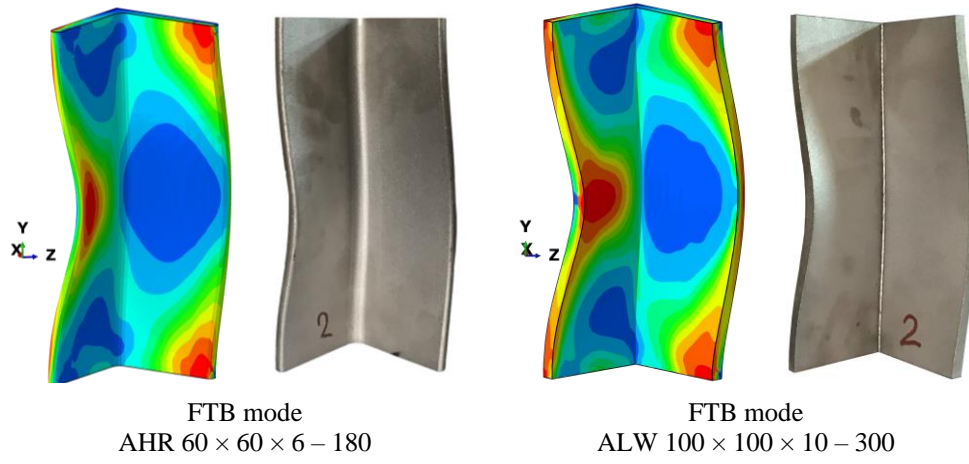
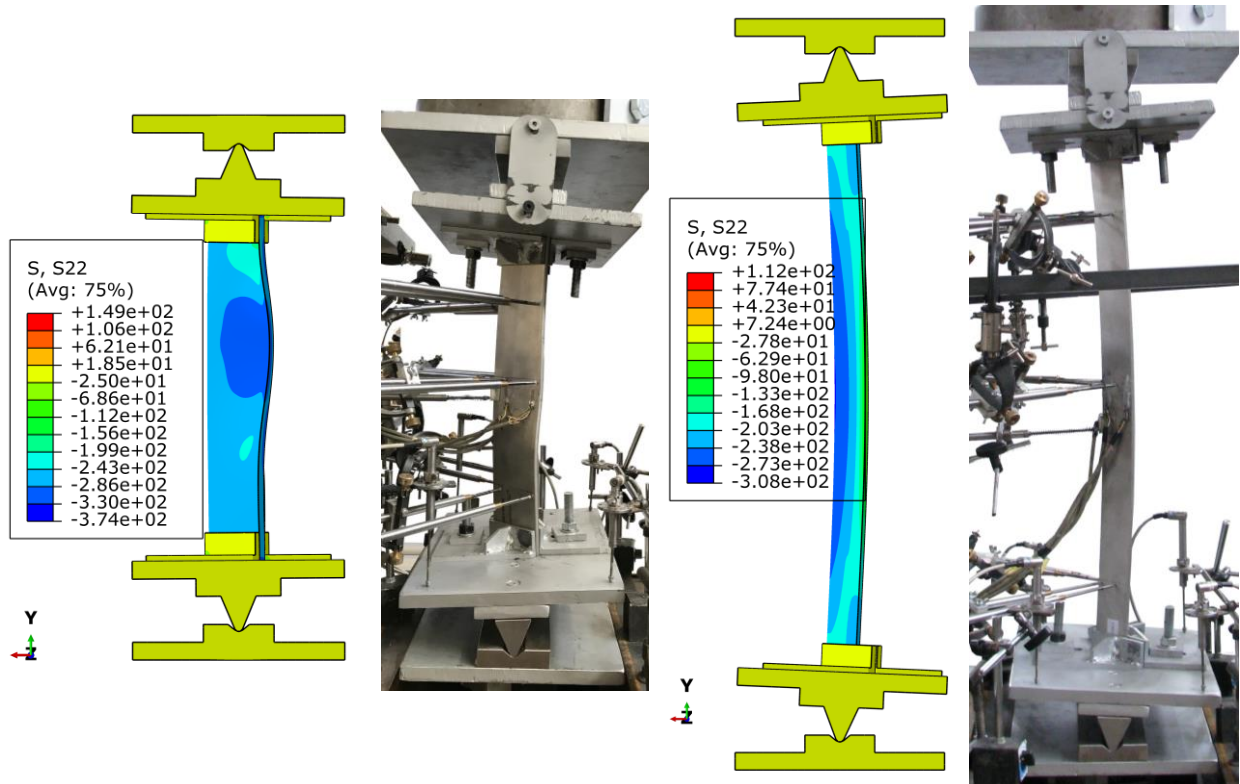
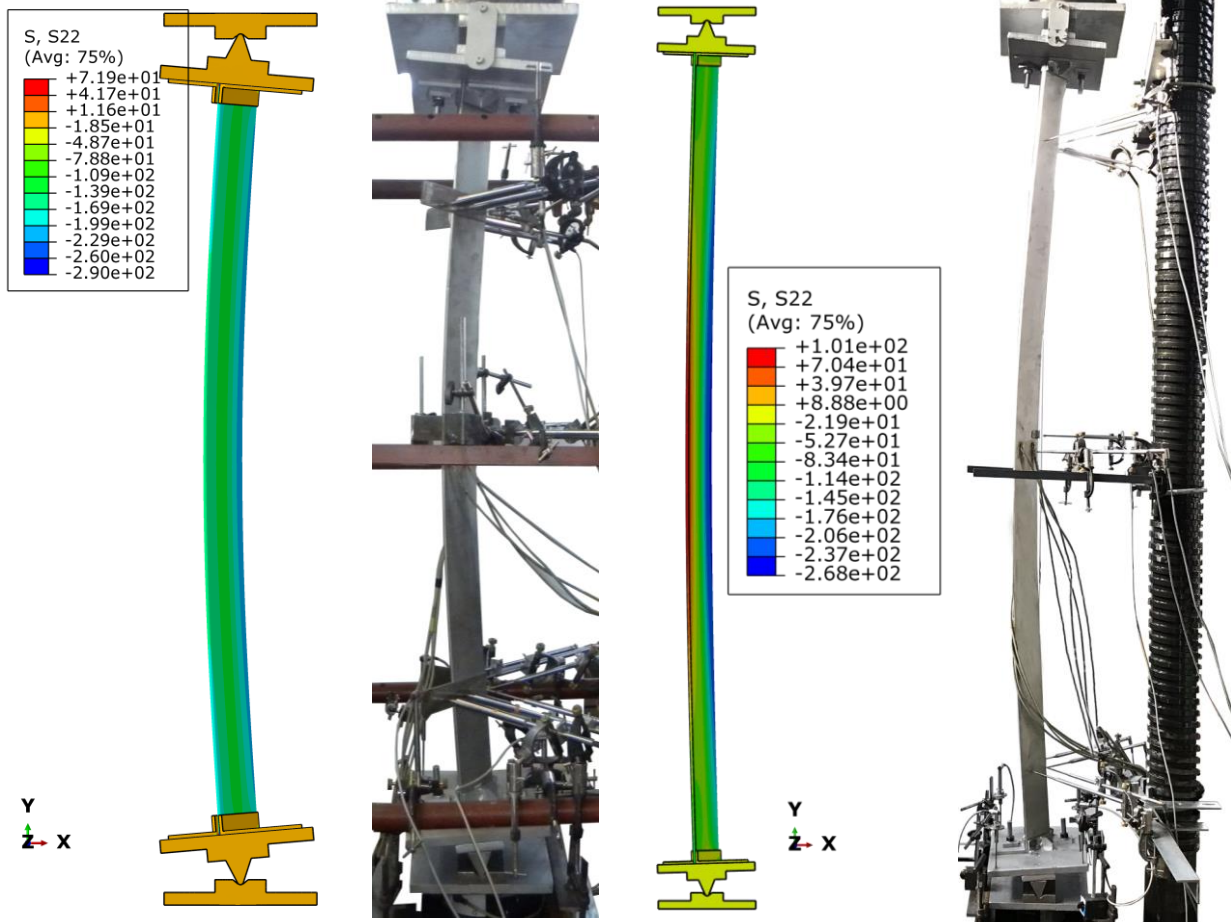


**Fig. 5** FE model and experimental [18], [19] buckling pattern of HRSS and LWSS angle stub columns.



minor-axis FB & FTB mode  
AHR 100 × 100 × 10 – 500 / short length column

minor-axis FB mode  
ALW 60 × 60 × 6 – 800 / intermediate length column



minor-axis FB mode

minor-axis FB mode

AHR 100 × 100 × 10 – 1500 / intermediate length column ALW 100 × 100 × 10 – 2500 / large length column  
**Fig. 6** FE model and experimental [18], [19] buckling patterns of HRSS and LWSS equal-leg angle columns.

In Fig. 7, Fig. 8 and Fig. 9, the axial compression versus axial deformation, the axial compression versus mid-height lateral deflection and the axial compression versus mid-height axial strain paths observed in the stub column tests and global buckling tests [18], [19] and those obtained from the FE modelling are compared for the selected HRSS and LWSS equal-leg angle columns, respectively. In the experiments performed by Filipović et al. [18], [19], the longitudinal axial strains were measured by strain gauges SG1–SG8, placed at the external and internal surfaces of the specimens' mid-height cross-sections. The FE nodes corresponding to the same positions of these strain gauges were used to record longitudinal axial strains in FE models. The lateral deflections about the cross-section minor-principal axis were experimentally monitored by means of displacement transducer LVDT7 placed at the angle-section heel at the mid-height of the specimens. The FE node corresponding to this displacement transducer was used to record lateral deflections of FE models. As can be seen from the figures, the correlation between the experimentally and numerically obtained buckling features, in terms of curve shapes, initial stiffness, deformation capacity, ultimate resistance and post-buckling responses, is very good.

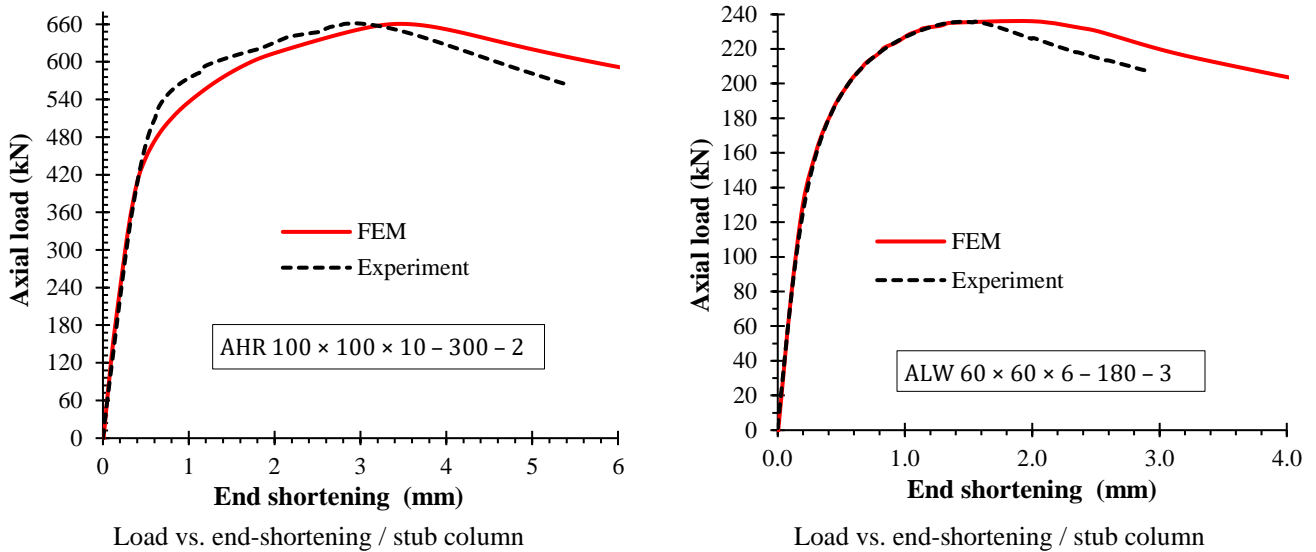
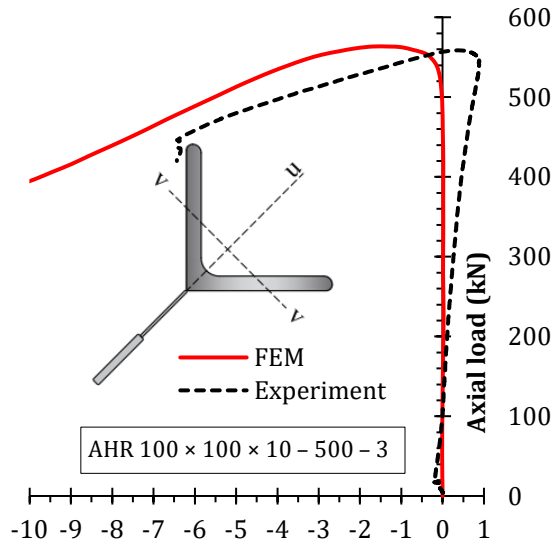
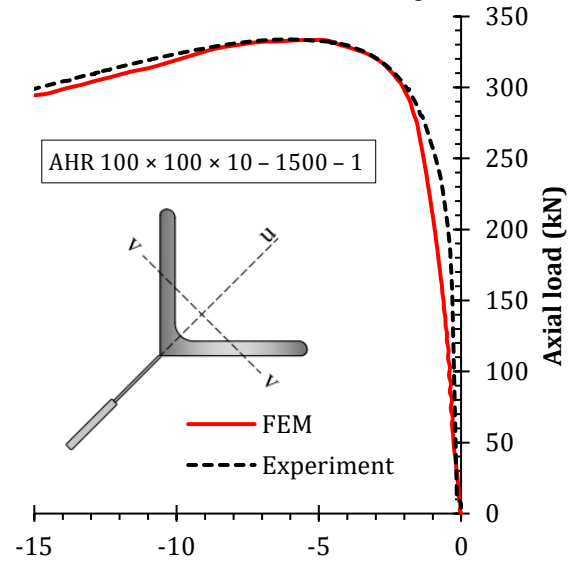


**Fig. 7** Comparison between experiments [18], [19] and FE modelling for HRSS and LWSS angle columns.



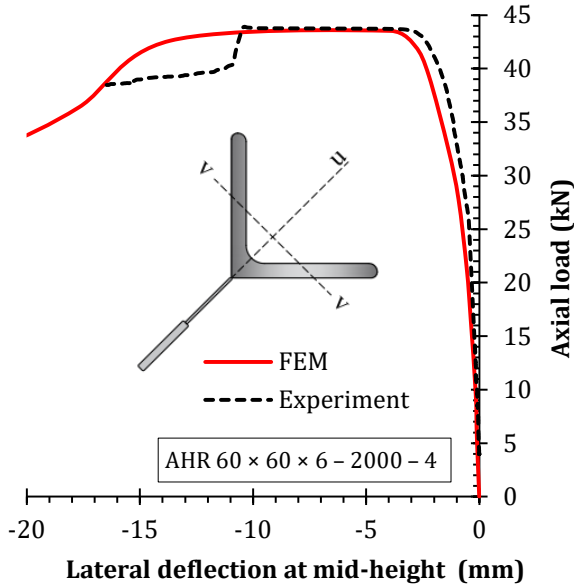
**Lateral deflection at mid-height (mm)**

Load vs. lateral deflections / short length column



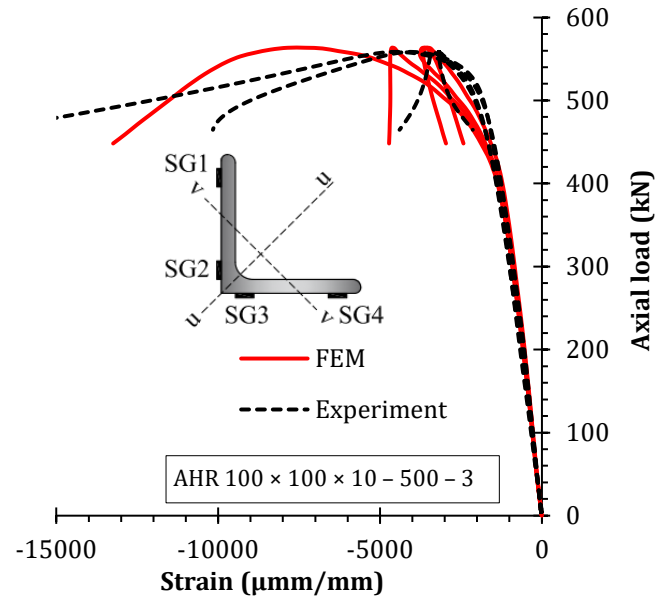
**Lateral deflection at mid-height (mm)**

Load vs. lateral deflections / intermediate length column



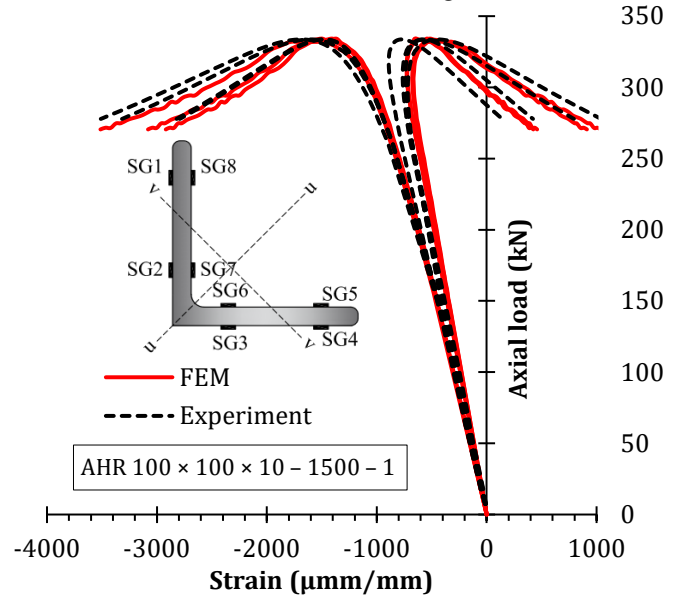
**Lateral deflection at mid-height (mm)**

Load vs. lateral deflection / large length column



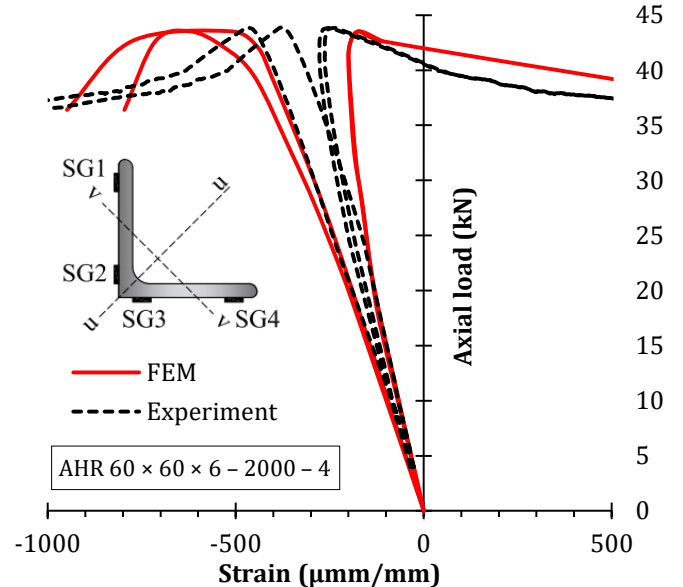
**Strain (μmm/mm)**

Load vs. axial strains / short length column



**Strain (μmm/mm)**

(a) Load vs. axial strains / intermediate length column

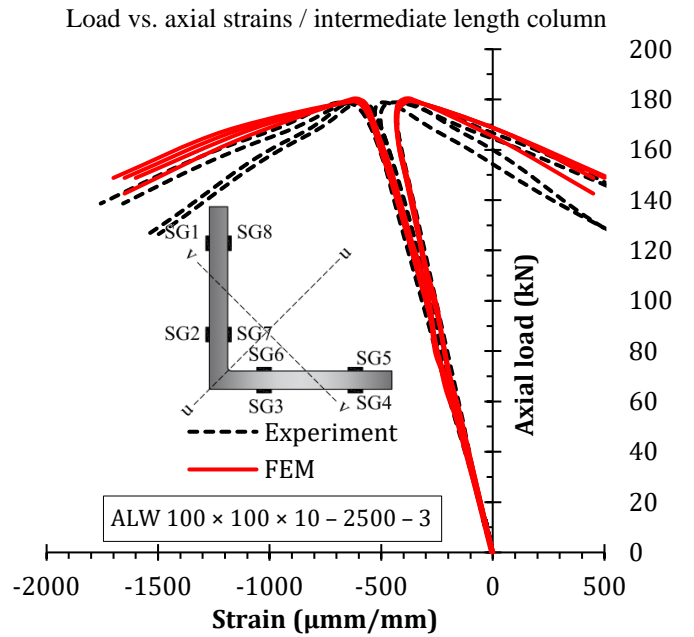
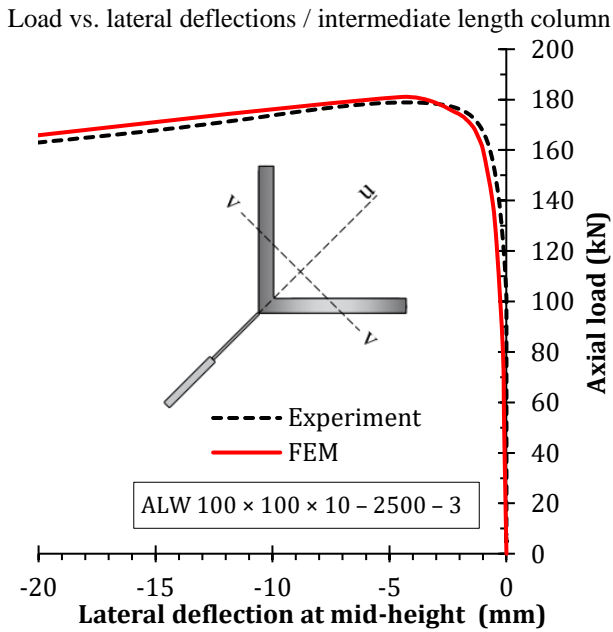
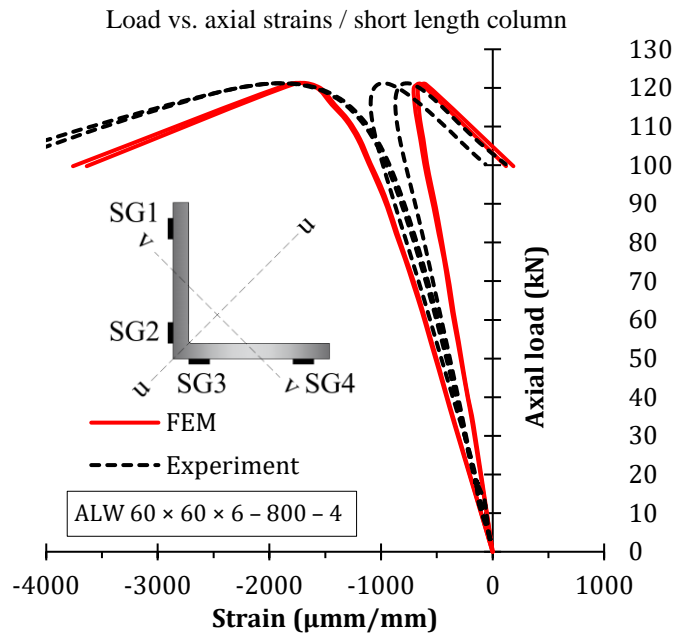
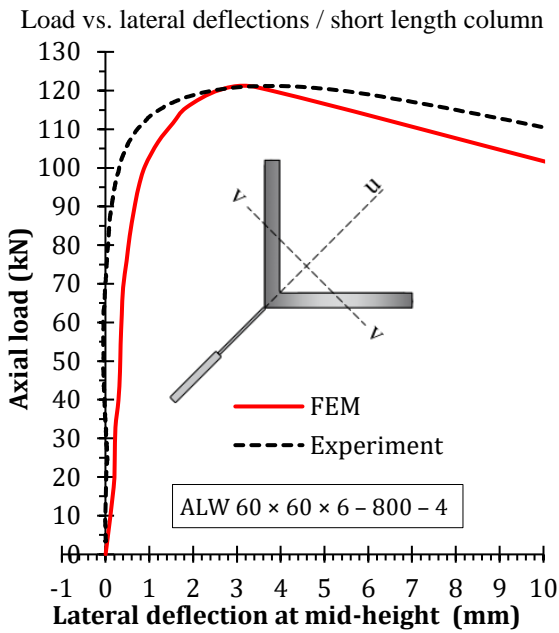
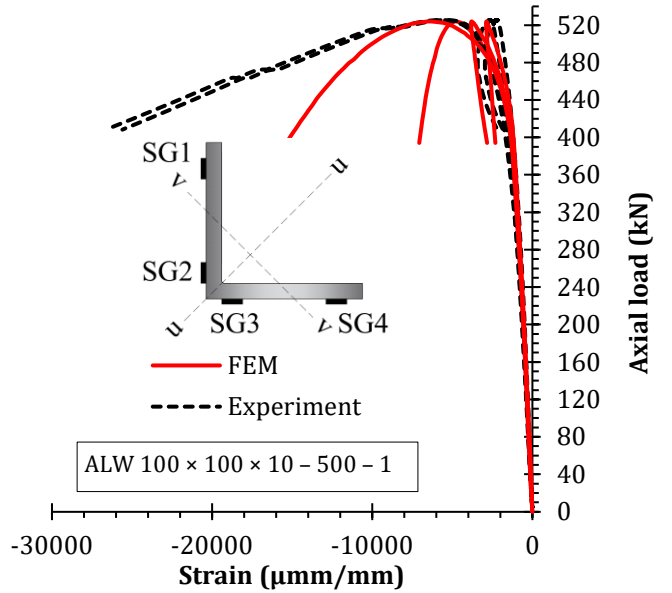
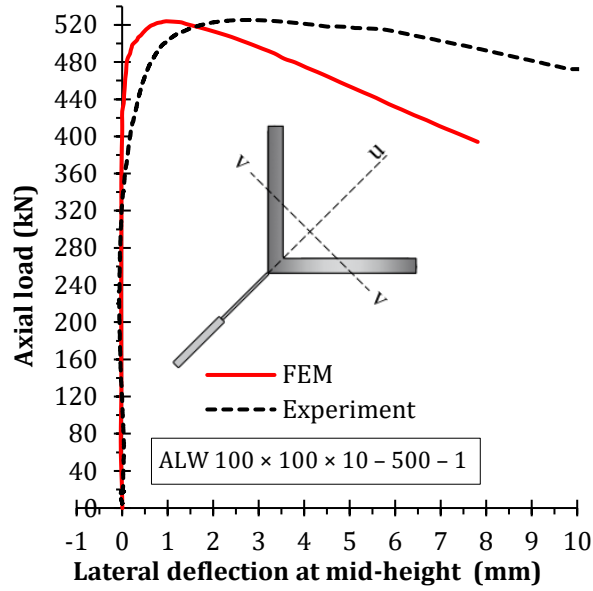


**Strain (μmm/mm)**

Load vs. axial strains / large length column

**Fig. 8** Comparison between experiments [18] and FE modelling for HRSS angle columns.





Load vs. lateral deflection / large length column

Load vs. axial strains / large length column

**Fig. 9** Comparison between experiments [19] and FE modelling for LWSS angle columns.



The ultimate buckling loads of the specimens  $N_{b,u,exp}$  [18], [19] are compared with those determined through the FE modelling in this study  $N_{b,u,FEM}$ , in Table 3 and Table 4 for HRSS and LWSS equal-leg angle columns, respectively. As can be seen from the tables, the ultimate strengths obtained from the FE models and the experiments are in close agreement; the average value of the FE model-to-experiments ultimate load ratio  $N_{b,u,FEM}/N_{b,u,exp}$  equals 0.97 and the coefficient of variation (CoV) is 6.62% for HRSS equal-leg angle columns, whereas these values are 0.98 and 7.69%, respectively, for LWSS equal-leg angle columns.

**Table 3.** Ultimate buckling load for HRSS angle columns – experiments [18] and FE modelling.

FE models / Specimens Designations as in [18]	Experiment					FE models $N_{b,u,FEM}$	Ratio $N_{b,u,FEM}/N_{b,u,exp}$
	Repeated tests				Average value $N_{b,u,exp}$		
	1	2	3	4			
AHR 60 × 60 × 6 – 180	301.3	298.2	292.5	-	297.3	257.1	0.86
AHR 60 × 60 × 6 – 800	163.9	145.1	172.2	151.6	158.2	159.6	1.01
AHR 60 × 60 × 6 – 2000	38.0	47.1	64.4	43.8	48.3	43.5	0.90
AHR 100 × 100 × 10 – 300	659.6	661.7	595.6	-	638.9	660.4	1.03
AHR 100 × 100 × 10 – 500	466	671.7	558.7	595.2	572.9	563.4	0.98
AHR 100 × 100 × 10 – 1500	333.7	290.2	423.0	289.4	334.1	334.0	1.00
AHR 100 × 100 × 10 – 2500	182.9	188.9	181.8	204.7	186.5	190.2	1.02
Mean							0.97
CoV (%)							6.62

**Table 4.** Ultimate buckling load for LWSS angle columns – experiments [19] and FE modelling.

FE models / Specimens Designations as in [19]	Experiment					FE models	Ratio
	Repeated tests				Average value		
	1	2	3	4			
					$N_{b,u,exp}$	$N_{b,u,FEM}$	$N_{b,u,FEM}/N_{b,u,exp}$
ALW 60 × 60 × 6 – 180	250.3	239.0	235.7	-	241.7	233.9	0.97
ALW 60 × 60 × 6 – 800	116.6	113.3	122.3	121.2	118.4	120.9	1.02
ALW 60 × 60 × 6 – 2000	29.3	31.2	55.9	56.6	43.3	35.9	0.83
ALW 100 × 100 × 10 – 300	671.1	646	630.6	-	649.2	638.4	0.98
ALW 100 × 100 × 10 – 500	525.3	532.1	520.1	518.8	524.1	523.8	1.00
ALW 100 × 100 × 10 – 1500	311.3	296.5	285.0	284.0	294.2	302.5	1.03
ALW 100 × 100 × 10 – 2500	145.6	156.2	178.8	194.4	168.8	179.8	1.07
Mean							0.98
CoV (%)							7.69

### 3. Imperfection sensitivity study

The development of design curves for steel columns is based on the assumption that initial geometric imperfections are equal to the maximum allowable fabrication and erection tolerances prescribed in the appropriate codes. Evaluation of the maximum compressive strengths of both straight, without residual stresses columns and initially imperfect columns are presented in this section, considering several combinations of geometric imperfection modes and residual stress distributions. The imperfection sensitivity study addresses pin-ended HRSS equal-leg angle columns and LWSS equal-leg angle columns, both with

nominal cross-section dimensions  $100 \times 100 \times 10$  mm and different lengths covering the nondimensional column slenderness range  $\bar{\lambda}_v$  about minor-axis from 0.295 to 2.441. The geometry of FE models was developed based on nominal column dimensions using hexahedron solid elements C3D8R with a global element size ranging from 2 to 3 mm. In contrast to the realistic and explicit FE modelling of BCs of tested columns described in Section 2, the pin-ended support conditions were herein modelled by theoretical, idealized hinges, since design criteria covering column buckling commonly establish the general case with this type BCs. The hinge-supported behaviour of the columns was established using kinematic coupling constraints. The nodes within the end sections were constrained to a reference point located at the centroid of the end cross-sections where the boundary conditions were defined. Failure loading is applied as displacement-controlled to a reference point in the loading zone.

The material models developed on the basis of tensile tests performed on coupons extracted from HRSS and LWSS equal-leg angle columns [18], [19], as in FE modelling in Section 2, were assigned to each FE model. Residual stresses were incorporated into the FE models using the generic residual stress patterns both for HRSS and LWSS equal-leg angle sections shown in Fig. 3. The residual stresses were applied to the FE models within a separate step finalised with the achievement of the equilibrium prior to the application of the failure loading, as described in Section 2.

The superposition of initial geometric imperfections in the shape of the lowest flexural-torsional mode and the lowest minor-axis FB mode was assigned to all FE models. For the flexural-torsional imperfections, the imperfection magnitude  $\omega_0$  was selected to correspond to 80% of the maximum permitted out-of-squareness specified in EN 10056-2 [33] (1 mm for angles with leg widths  $c \leq 100$  mm, 1.5 mm for  $100 < c \leq 150$  mm, 2 mm for  $150 < c \leq 200$  mm and 3 mm for  $c > 200$  mm). The adopted amplitude value of global bow imperfections (minor-axis FB mode)  $\delta_0 = L/1000$  ( $L$  is the column length) corresponds to 75% of the maximum permitted imperfections for essential tolerances according to EN 1090-2 [34]. The reductions of geometric imperfection amplitudes are in accordance with provisions stated in Annex C of EN 1993-1-5 [35]. Considering that the sign of initial imperfections is not explicitly defined in Technical requirements [33], [34], and it is not obvious without previous measurements, evaluation of imperfection effects was performed considering both directions of imperfection distributions: positive directions associated with deformed

buckling shapes of FE models observed in the LBA and negative directions that are opposite from the directions of the deformed buckling shapes of FE models in the LBA. The positive sign of torsional imperfections corresponds to cross-section rotation in the clockwise direction (see Fig. 10a), whereas the positive sign of global imperfections corresponds to the deformed column which bends out towards the heel of the angle section (tensile yielding in the region of angle heel), see Fig. 10b.

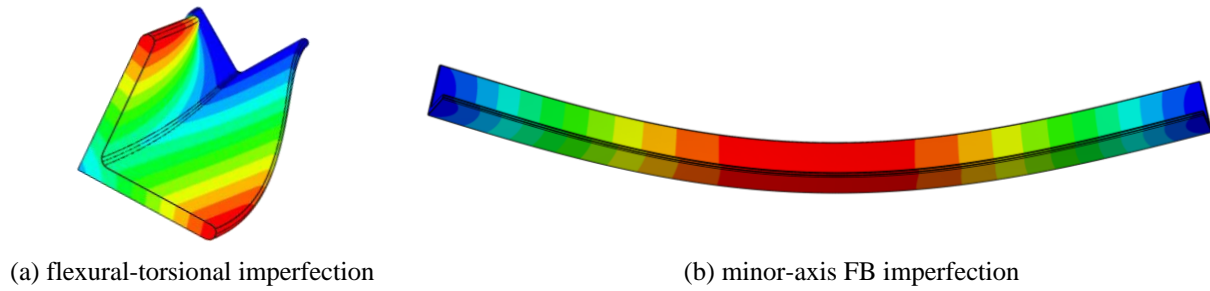


**Fig. 10** Distribution patterns of initial geometric imperfections with a positive sign.

The imperfection sensitivity study presented herein accounts for separate and combined effects of initial geometric imperfections and residual stresses on ultimate buckling loads of both HRSS and LWSS equal-leg angle columns. The compressive capacities of imperfect FE models ( $N_{b,u,imperfect}$ ) affected by initial geometric imperfections and residual stresses are compared with compressive capacities of the equivalent initially straight FE models without residual stresses ( $N_{b,u,straight}$ ). Table 5 and Table 6 quantify the decrease of strength of initially perfect columns caused by separate and combined actions of geometric imperfections (GI) accounting for the change of their distribution signs and residual stresses (RS). The non-dimensional slenderness  $\bar{\lambda}_v = \sqrt{Af_y/N_{cr,FB,v}}$ , listed in Table 5 and Table 6, relates to the minor-axis flexural buckling mode.

In order to investigate the effects of varying the imperfection controlling parameters on the ultimate column strength, the load–lateral deflection curves about the cross-section minor-axis at mid-height of the analysed HRSS and LWSS columns ( $L = 1500$  mm) are presented in Fig. 11 and Fig. 12, respectively, whereas the corresponding distributions of axial stresses at the ultimate limit state along the critical mid-height cross-sections of these columns are shown in Fig. 13 and 14, respectively.

**Table 5.** Quantification of initial GI and RS influences on FE ultimate buckling loads for HRSS angles.

FE models / Designations as in [18]	$N_{b,u,imperfect} / N_{b,u,straight}$ Individual effects of GI and RS	Combined effects of GI and RS
--	---	----------------------------------

	Non-dimensional slenderness $\bar{\lambda}_v$	without GI & with RS	with +GI & without RS	with -GI & without RS	with +GI & with RS	with -GI & with RS
AHR 100 × 100 × 10 – 500	0.305	1.00	0.96	1.00	0.96	1.00
AHR 100 × 100 × 10 – 600	0.366	1.00	0.96	0.99	0.96	0.98
AHR 100 × 100 × 10 – 700	0.427	1.00	0.98	0.98	0.98	0.98
AHR 100 × 100 × 10 – 800	0.488	1.00	0.95	0.97	0.95	0.96
AHR 100 × 100 × 10 – 900	0.549	1.00	0.95	0.96	0.94	0.94
AHR 100 × 100 × 10 – 1000	0.610	1.00	0.94	0.95	0.93	0.93
AHR 100 × 100 × 10 – 1200	0.732	1.00	0.92	0.93	0.90	0.90
AHR 100 × 100 × 10 – 1300	0.793	0.98	0.90	0.92	0.87	0.87
AHR 100 × 100 × 10 – 1400	0.854	0.95	0.86	0.88	0.84	0.83
AHR 100 × 100 × 10 – 1500	0.915	0.93	0.82	0.84	0.80	0.79
AHR 100 × 100 × 10 – 1600	0.976	0.92	0.80	0.81	0.77	0.76
AHR 100 × 100 × 10 – 1700	1.037	0.92	0.79	0.80	0.76	0.75
AHR 100 × 100 × 10 – 1800	1.098	0.96	0.80	0.81	0.77	0.75
AHR 100 × 100 × 10 – 2000	1.220	0.94	0.82	0.84	0.79	0.78
AHR 100 × 100 × 10 – 2200	1.342	0.93	0.83	0.84	0.79	0.78
AHR 100 × 100 × 10 – 2400	1.464	0.89	0.78	0.79	0.77	0.72
AHR 100 × 100 × 10 – 2500	1.525	0.85	0.74	0.76	0.72	0.70
AHR 100 × 100 × 10 – 2600	1.586	0.82	0.70	0.72	0.71	0.69
AHR 100 × 100 × 10 – 2800	1.708	0.83	0.67	0.68	0.67	0.62
AHR 100 × 100 × 10 – 3000	1.831	0.79	0.63	0.65	0.65	0.62
AHR 100 × 100 × 10 – 3200	1.953	0.74	0.61	0.62	0.66	0.60
AHR 100 × 100 × 10 – 3400	2.075	0.75	0.59	0.60	0.63	0.52
AHR 100 × 100 × 10 – 3500	2.136	0.76	0.57	0.58	0.61	0.53
AHR 100 × 100 × 10 – 3600	2.197	0.76	0.56	0.57	0.59	0.52
AHR 100 × 100 × 10 – 3800	2.319	0.75	0.53	0.54	0.56	0.50
AHR 100 × 100 × 10 – 4000	2.441	0.72	0.50	0.51	0.55	0.47

**Table 6.** Quantification of initial GI and RS influences on FE ultimate buckling loads for LWSS angles.

FE models / Designations as in [19]	Non- dimensional slenderness $\bar{\lambda}_v$	$N_{b,u,imperfect} / N_{b,u,straight}$				
		Individual effects of GI and RS			Combined effects of GI and RS	
		without GI & with RS	with +GI & without RS	with -GI & without RS	with +GI & with RS	with -GI & with RS
ALW 100 × 100 × 10 – 500	0.295	1.00	0.94	0.98	0.94	0.98
ALW 100 × 100 × 10 – 600	0.354	1.00	0.95	0.97	0.95	0.96
ALW 100 × 100 × 10 – 700	0.413	0.99	0.95	0.96	0.95	0.95
ALW 100 × 100 × 10 – 800	0.472	0.98	0.94	0.92	0.93	0.93
ALW 100 × 100 × 10 – 900	0.531	0.97	0.94	0.94	0.93	0.92
ALW 100 × 100 × 10 – 1000	0.591	0.97	0.94	0.94	0.93	0.92
ALW 100 × 100 × 10 – 1200	0.709	0.95	0.91	0.91	0.89	0.87
ALW 100 × 100 × 10 – 1300	0.768	0.92	0.88	0.88	0.86	0.83
ALW 100 × 100 × 10 – 1400	0.827	0.89	0.84	0.84	0.82	0.79
ALW 100 × 100 × 10 – 1500	0.886	0.86	0.79	0.80	0.78	0.75
ALW 100 × 100 × 10 – 1600	0.945	0.82	0.76	0.76	0.74	0.71
ALW 100 × 100 × 10 – 1700	1.004	0.81	0.74	0.74	0.73	0.69
ALW 100 × 100 × 10 – 1800	1.063	0.81	0.75	0.75	0.72	0.69
ALW 100 × 100 × 10 – 2000	1.181	0.81	0.78	0.76	0.77	0.68
ALW 100 × 100 × 10 – 2200	1.299	0.78	0.75	0.75	0.76	0.67
ALW 100 × 100 × 10 – 2400	1.417	0.73	0.72	0.72	0.71	0.66
ALW 100 × 100 × 10 – 2500	1.476	0.73	0.69	0.69	0.69	0.60
ALW 100 × 100 × 10 – 2600	1.535	0.70	0.64	0.64	0.64	0.60
ALW 100 × 100 × 10 – 2800	1.653	0.64	0.59	0.59	0.62	0.50
ALW 100 × 100 × 10 – 3000	1.772	0.64	0.55	0.55	0.56	0.50
ALW 100 × 100 × 10 – 3200	1.890	0.57	0.51	0.51	0.57	0.47
ALW 100 × 100 × 10 – 3400	2.008	0.52	0.47	0.47	0.56	0.45
ALW 100 × 100 × 10 – 3500	2.067	0.52	0.46	0.46	0.54	0.38
ALW 100 × 100 × 10 – 3600	2.126	0.52	0.45	0.45	0.52	0.38
ALW 100 × 100 × 10 – 3800	2.244	0.52	0.43	0.42	0.48	0.38
ALW 100 × 100 × 10 – 4000	2.362	0.50	0.39	0.39	0.45	0.36

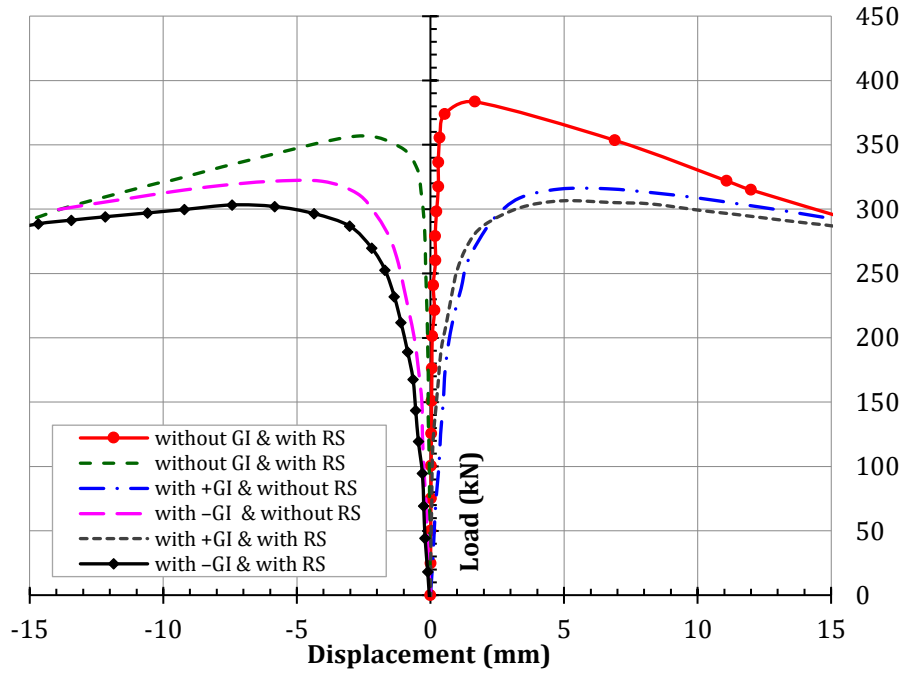


**Fig. 11** Load–lateral deflection curves about minor-axis at mid-height of FE model AHR  $100 \times 100 \times 10 - 1500$ .

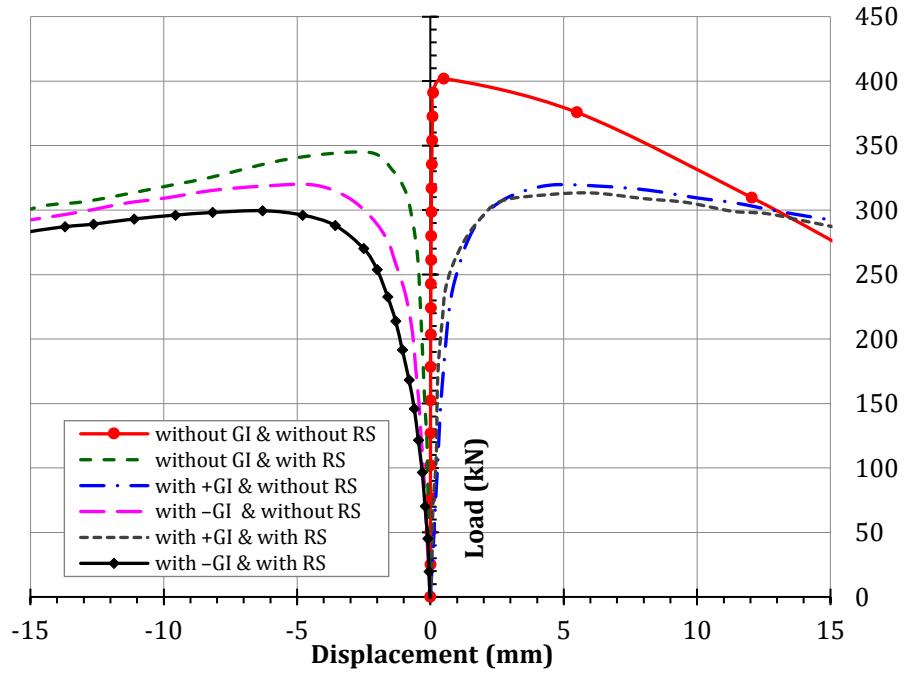


**Fig. 12** Load–lateral deflection curves about minor-axis at mid-height of FE model ALW  $100 \times 100 \times 10 - 1500$ .

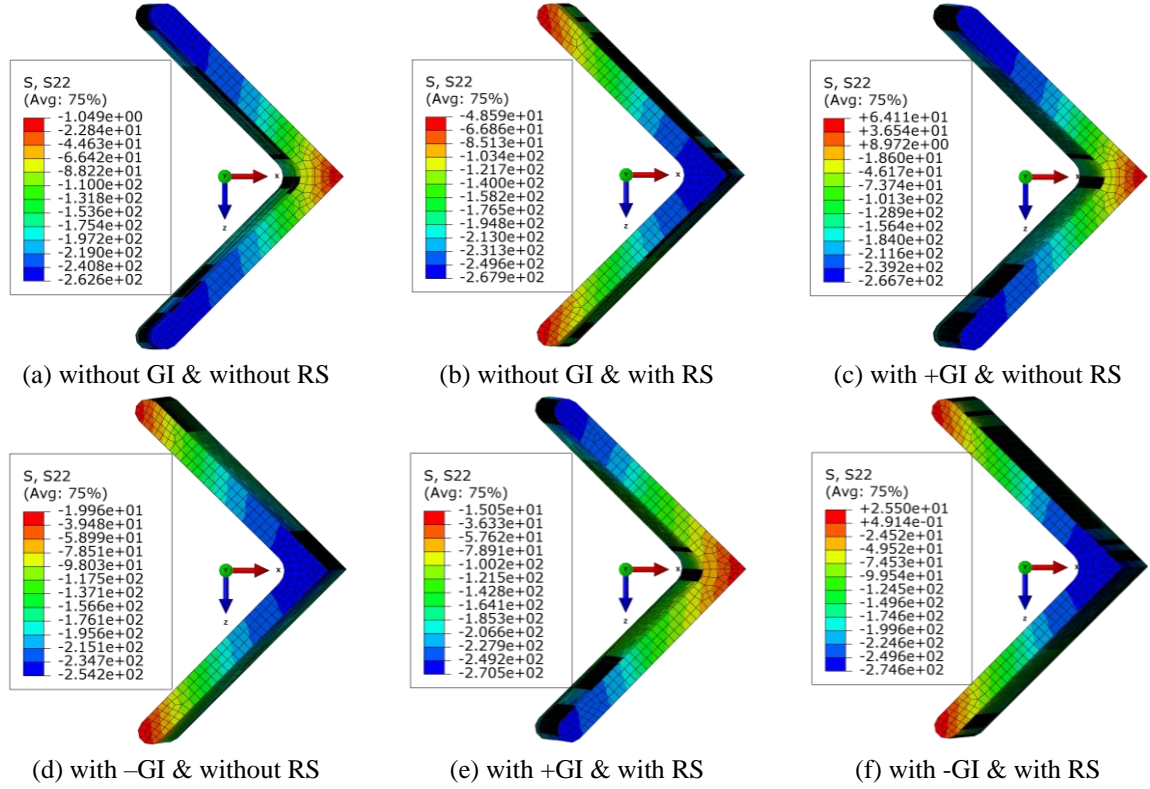


**Fig. 13** Distributions of axial stresses along mid-height cross-section of FE model AHR  $100 \times 100 \times 10 - 1500$  at ultimate limit state.

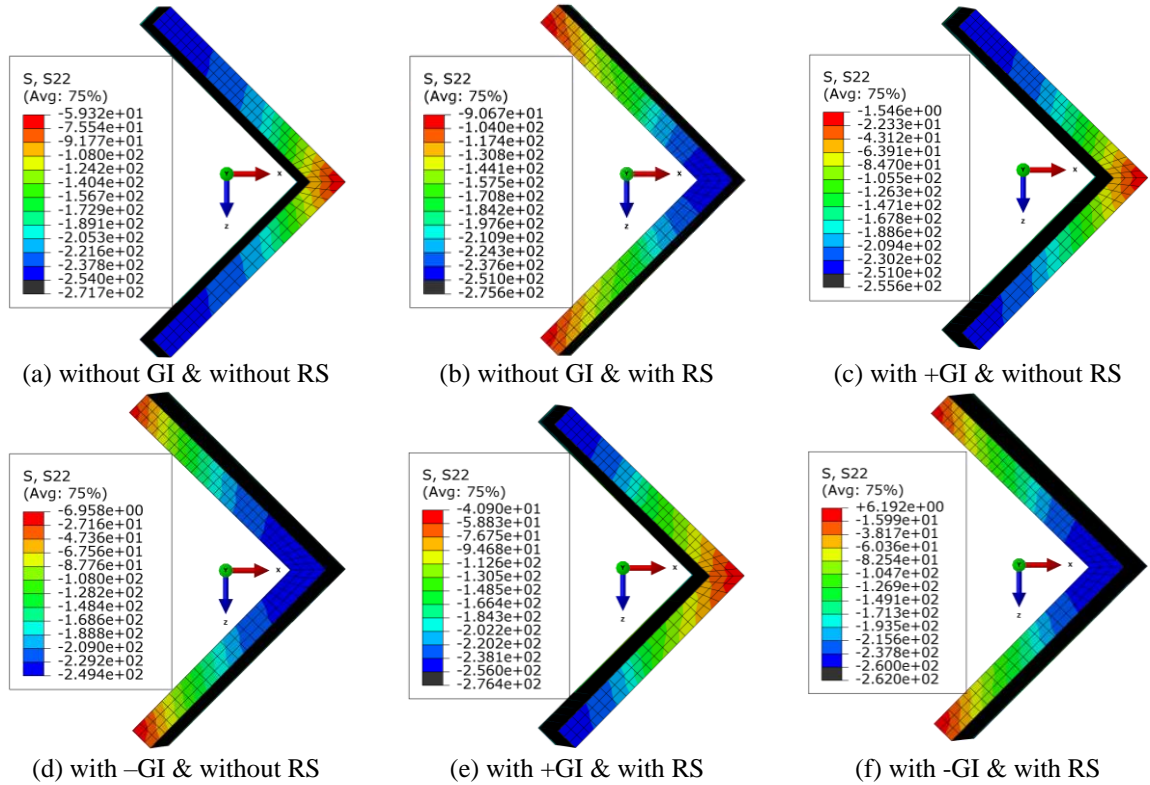


**Fig. 14** Distributions of axial stresses along mid-height cross-section of FE model ALW  $100 \times 100 \times 10 - 1500$  at ultimate limit state.

Based on the obtained results, a brief discussion is presented below:

- The individual actions of residual stresses do not influence the HRSS angle column compressive capacities in the low and intermediate slenderness range up to  $\bar{\lambda}_v = 0.793$ , whereas the LWSS angle columns are not susceptible to individual actions of residual stresses in the low slenderness range up to  $\bar{\lambda}_v = 0.472$ . On the contrary, in the higher slenderness range, the maximum decrease of the ultimate buckling resistance of initially straight columns, solely caused by residual stresses, is 38% for hot-rolled and 50% for laser-welded angle sections.
- The flexural-torsional imperfection does not have any noticeable effect on buckling behaviour of both HRSS and LWSS angle columns in the intermediate and high slenderness range. The ultimate structural response of the columns does not depend on the flexural-torsional amplitude sign.
- As expected, the minor-axis bow imperfections more adversely affect column strength in comparison with residual stresses. As can be seen from Table 5 and Table 6, the weakening effects of both amplitude signs of minor-axis FB shape of initial geometric imperfections ( $+L/1000$  and  $-L/1000$ ) are similar: the reduction the compressive strength of perfectly straight HRSS angle columns is from 4% in the low slenderness range and 49% in the higher slenderness range, whereas the decrease in strength is more marked for LWSS angles with a range from 2% for short length columns up to 61% for large length angle columns.
- When combined, residual stresses and geometric imperfections do not achieve the sum of their separate effects on the column buckling resistances, see Fig. 13 and Fig. 14. Moreover, as can be seen from Table 5 and Table 6, the combined effects are not significantly higher than those produced by the individual action of the initial geometric imperfections. However, it should be noted that the impact of the sign of the initial imperfection minor-axis flexural component is more relevant when their effects are considered in conjunction with effects of residual stresses. The results indicate that interaction effects of residual stresses and negative distribution of global initial geometric imperfections with an amplitude of  $-L/1000$  in combination with flexural-torsional imperfections with

amplitudes that correspond to 80% of the maximum permitted cross-section tolerances specified in EN 10056-2 [33], generally leads to the lowest values of ultimate buckling loads both from HRSS and LWSS angle columns. The exception is observed for short length angle columns where interaction effects of residual stresses and positive distributions of initial geometric imperfections are somewhat more pronounced.

- The LWSS angle columns are more sensitive to residual stresses and geometric imperfections effects than HRSS angle columns. In comparison with equivalent HRSS angle columns, the drop of compressive capacities of initially straight LWSS angle columns are higher up to 2% in the low slenderness ( $\bar{\lambda}_v = 0.305$ ), 6% in the intermediate slenderness ( $\bar{\lambda}_v = 1.037$ ), and 11% in the high slenderness range ( $\bar{\lambda}_v = 2.441$ ).

By observing the equilibrium paths for HRSS and LWSS columns, presented in Fig. 11 and Fig. 12, respectively, it can be noticed that, in the absence of residual stresses, the change of sign of the minor-axis bow imperfections changes the direction of column lateral deflections about the minor-axis at the critical mid-height cross-sections. However, the variation of ultimate loads is not particularly pronounced (see Table 5 and Table 6). This outcome deviates from results of the research performed on CFSS equal-leg angle columns by Dobrić et al. [24], where it was found that the change of sign of the minor-axis bow imperfections can significantly reduce the column compressive capacities. In the context of interpreting these discrepancies, a comparative analysis of the structural responses of the HRSS and LWSS equal-leg angle columns investigated in this paper and the CFSS columns studied by Dobrić et al. [24], all containing initial imperfections, was performed for the considered ranges of angle-section geometric dimensions (see Section 4) and pin-ended boundary conditions. The conclusions of this comparative analysis can be summarized as follows:

- (i) For the same nominal cross-section dimensions involving width and thickness of angle-section legs, the moments of inertia about the principal minor-axis of both HRSS and LWSS angle-sections are approximately 28% higher than those obtained for CFSS angle-sections, considering differences in the shapes of cross-section corner regions. The direction of minor-axis lateral deflections of both



HRSS and LWSS angle columns without imperfections (see Fig. 13a and Fig. 14a) is the same as it was predicted by LBA for the critical minor-axis FB mode (see Fig. 10b). However, the distance between the cross-section centroid and the extreme fibre of the angle heel  $u_1$  is higher than the distance between the cross-section centroid and the extreme fibres of the leg tips  $u_2$ , along the major principal axis — the ratio  $u_1/u_2$  (see Fig. 15) ranges from 1.06 to 1.16 for HRSS angles, and from 1.06 to 1.12 for LWSS angles. Consequently, the elastic minor-axis section modulus for the extreme fibres of leg tips is greater than that corresponding to the extreme fibre of the angle heel (with respect to introduced bending moment). In addition, the cross-section part areas  $A_1$  and  $A_2$  related to minor-axis (see Fig. 15) are approximately equal (the difference is up to 0.6%). Hence, the influence of bending stiffness of HRSS and LWSS equal-leg angle columns could increase the column sensitivity to minor-axis flexural imperfections with a positive amplitude sign (+GI).

However, individual effects of both geometric minor-axis flexural imperfections with a negative amplitude sign (−GI) and residual stresses cause the columns to bend out towards the leg tips with the maximum compressive stresses in the area of the angle-section heel, see Fig. 13b, Fig. 13d for HRSS columns and Figs. Fig. 14b and Fig. 14d for LWSS columns. Consequently, the same direction of the minor-axis lateral deflections occurs because of the combined effects of geometric imperfections and residual stresses; however, the tensile stresses occur in the leg tip areas, whereas the compressive stresses in the area of the angle heel are higher than those that occur herein due to their individual effects (see Fig. 13f and Fig. 14f).

The individual effect of geometric imperfections with a positive amplitude sign (+GI) causes the columns to bend out towards the angle heel with maximum compressive stresses in the leg tip areas (see Figs. 13c and 14c for HRSS and LWSS columns, respectively). Considering that the influence of geometric imperfections on the ultimate column resistance is more significant than the influence of residual stresses (see Table 5 and Table 6), and that the positive minor-axis bow imperfections cause lateral deflections of column and a stress distribution in the critical cross-section with the opposite sign to those caused by influence of residual stresses, it can be concluded that the interactive effects of positive geometric imperfections (+GI) and residual stresses lead to a lower reduction of the

ultimate buckling load of the equivalent initially perfect column than the combined effects of negative geometric imperfections ( $-GI$ ) and residual stresses.

- (ii) The deformed shape of CFSS equal-leg angle columns for the critical minor-axis FB mode, predicted by LBA [24] is characterised by the direction of minor-axis lateral deflections that is opposite in sign compared with that of the critical minor-axis FB mode of HRSS and LWSS angles. Moreover, unlike in HRSS and LWSS angle columns, for CFSS angle columns, the distance between the cross-section centroid and the extreme fibre of the angle heel  $u_1$  is lower than the distance between the cross-section centroid and the extreme fibres of the leg tips  $u_2$ , along the major principal axis — the ratio  $u_1/u_2$  (see Fig. 15) ranges from 0.85 to 0.97. Therefore, the elastic minor-axis section modulus for the extreme fibres of the leg tips is lower than that corresponding to the extreme fibre of the angle heel (with respect to the introduced bending moment). In addition, the cross-section area  $A_1$  can be up to 3.5% higher than the cross-section area  $A_2$ , depending on the internal corner radius  $r_i$  (see Fig. 15). Hence, the influence of bending stiffness in CFSS area equal-leg angle columns could increase the column sensitivity to minor-axis flexural imperfections with a negative amplitude sign ( $-GI$ ). Note also that several studies [36], [37] have shown that the influence of residual stresses on the ultimate resistances of CFSS columns may be neglected, indicating that the ultimate compressive capacity of CFSS equal-leg angle column is dominantly affected by the variation of the initial geometric imperfections.

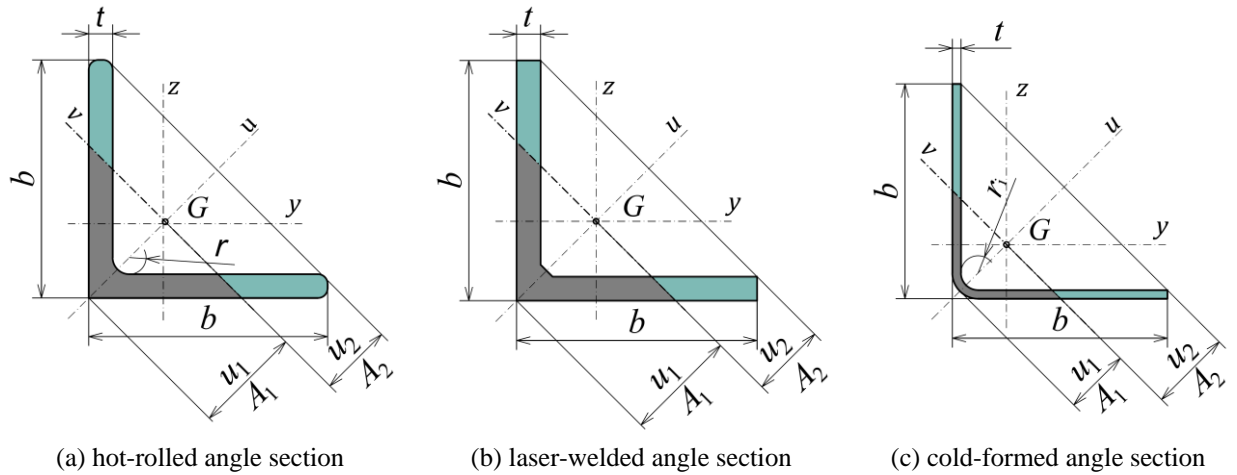


**Fig. 15** Cross-section geometry.

#### 4. Numerical parametric study

Experimentally verified nonlinear FE modelling was used to perform an extensive FE parametric study aiming to thoroughly examine the structural responses of HRSS and LWSS equal-leg angle columns and develop a framework for their reliability-based design. Similar to previous work performed on cold-formed equal-leg angles [24], the study addresses the behaviour of fixed-ended short length columns to predict their cross-section resistances and assess the plateau length of buckling curves, and the behaviour of pin-ended slender columns to predict their major-axis FTB and minor-axis FB capacities, as well as to derive buckling curves for their design.

In total, 15 and 17 different section dimensions were selected for HRSS and LWSS equal-leg angle columns, respectively, to generate a range of local slenderness covering both slender and non-slender cross-sectional behaviour according to the slenderness limits set out in EN 1993-1-4 [1]. A summary of the considered column geometries of HRSS and LWSS angles are provided in Table 7 and Table 8, respectively.

**Table 7.** Cross-section geometries and lengths of HRSS angle columns included in the FE study.

Equal-leg angle section	Column length $L$ (mm)	Leg width $b$ (mm)	Thickness $t$ (mm)	Internal radius $r_i$ (mm)
AHR 50 × 50 × 5	200–2000	50	5	7
AHR 60 × 60 × 6	300–2200	60	6	7
AHR 70 × 70 × 7	400–2800	70	7	9
AHR 80 × 80 × 8	400–3200	80	8	10
AHR 80 × 80 × 10	400–3000	80	10	9
AHR 90 × 90 × 6	400–3500	90	6	10
AHR 90 × 90 × 10	500–3400	90	10	11
AHR 100 × 100 × 10	500–4000	100	10	7.5
AHR 110 × 110 × 10	500–4400	110	10	13
AHR 120 × 120 × 12	500–4600	120	12	13
AHR 130 × 130 × 10	700–5000	130	13	14
AHR 130 × 130 × 16	600–4800	130	16	14
AHR 140 × 140 × 14	600–5400	140	14	15
AHR 150 × 150 × 15	700–5800	150	15	16
AHR 150 × 150 × 20	700–5800	150	20	16

**Table 8.** Cross-section geometries and lengths of LWSS angle columns included in the FE study.

Equal-leg angle section	Column length $L$ (mm)	Leg width $b$ (mm)	Thickness $t$ (mm)	Internal radius $r_i$ (mm)
ALW 50 × 50 × 5	200–2000	50	5	-
ALW 60 × 60 × 6	300–2200	60	6	-
ALW 70 × 70 × 7	400–2800	70	7	-
ALW 80 × 80 × 8	400–3200	80	8	-
ALW 80 × 80 × 10	400–3000	80	10	-
ALW 90 × 90 × 6	400–3500	90	6	-
ALW 90 × 90 × 10	500–3400	90	10	-
ALW 100 × 100 × 10	500–4000	100	10	-
ALW 110 × 110 × 10	500–4400	110	10	-
ALW 120 × 120 × 12	500–4600	120	12	-
ALW 130 × 130 × 10	700–5000	130	13	-
ALW 130 × 130 × 16	600–4800	130	16	-
ALW 140 × 140 × 14	600–5400	140	14	-

ALW 150 × 150 × 15	700-5800	150	15	-
ALW 150 × 150 × 20	700-5800	150	20	-
ALW 180 × 180 × 18	800-6000	180	18	-
ALW 250 × 250 × 20	1400-7000	250	20	-

The FE parametric study involved the same input parameters—stress-strain relationships, residual stresses, and BCs—as in the case of imperfection sensitivity study described in Section 3. The pattern, including a superposition of the flexural-torsional imperfection with the amplitude that corresponds to 80% of the maximum permitted cross-section tolerance [33] and a minor-axis FB imperfection with the amplitude of  $-L/1000$ , was used to assess the global stability of angle columns.

## 5. Assessment of existing design rules for stainless steel equal-leg angle columns

In this section, the European structural code EN 1993-1-4 [1] and the American Institute of Steel Construction (AISC) Design Guide 27 [16] are summarised and then assessed using the experimental data collected from literature [2], [3], [12], [13], [14], [15], [18], [19] and the numerical data obtained through the FE parametric study described in previous section.

### 5.1. European structural code EN 1993-1-4

In accordance with the carbon steel design standard EN 1993-1-1 [21], the supplementary rules provided in Clause 5.4.2.1 of EN 1993-1-4 [1] adopt the Perry-Robertson design approach for the verification of axially compressed members against buckling. The buckling resistance of a stainless steel compression member  $N_{b,Rd}$ , is obtained from Eq. (1):

$$N_{b,Rd} = \frac{\chi A f_y}{\gamma_{M1}} \quad (1)$$

where  $f_y$  is the material yield strength, taken as the 0.2% proof strength,  $A$  is the cross-sectional area, taken as the gross cross-sectional area for Class 1, 2 and 3 sections and an effective cross-sectional area  $A_{eff}$  for Class 4 sections, and  $\gamma_{M1}$  is the partial resistance factor for the member. The non-dimensional buckling reduction factor  $\chi$  is calculated using Eq. (2):

$$\chi = \frac{1}{\phi + \sqrt{\phi^2 - \bar{\lambda}^2}} \leq 1.0 \quad (2)$$

where  $\bar{\lambda}$  is the relevant non-dimensional column slenderness and  $\phi$  is defined as

$$\phi = 0.5(1 + \eta + \bar{\lambda}^2) \quad (3)$$

The non-dimensional column slenderness  $\bar{\lambda}$  is equal to the square root of the ratio of the yield load ( $N_y = A \cdot f_y$  for Class 1, 2 and 3 sections and  $N_y = A_{\text{eff}} \cdot f_y$  for Class 4 sections) to the elastic critical buckling load for the relevant buckling mode  $N_{\text{cr}}$ . The generalised imperfection factor  $\eta$  is determined using the following expression:

$$\eta = \alpha(\bar{\lambda} - \bar{\lambda}_0) \quad (4)$$

where  $\alpha$  is the imperfection factor and  $\bar{\lambda}_0$  is the non-dimensional limiting slenderness. According to Tables 6.1 and 6.2, Clause 6.3.1.2, EN 1993-1-1 [21], the buckling curve  $b$  ( $\alpha = 0.34$  and  $\bar{\lambda}_0 = 0.2$ ) should be used for the design of compressed carbon steel equal-leg angle columns. However, the existing code EN 1993-1-4 [1] does not state the values of the imperfection factor  $\alpha$  nor the limiting slenderness  $\bar{\lambda}_0$  for stainless steel angles, fabricated by hot-rolling and laser-welding processes, in the relevant buckling plane, primarily due to lack of research in this area.

The procedure for determining the effective widths for Class 4 cross-sections of stainless steel members is provided in Clause 5.2.3 of EN 1993-1-4 [1]. This procedure, which is based on the method for carbon steel sections stated in EN 1993-1-5 [35], includes modified and more conservative expressions for reduction factors, in comparisons with equivalent expressions for carbon steel, to account for the non-linear response of stainless steel. For columns with non-symmetric Class 4 cross-sections, the additional moment caused by the loss of cross-section effectivity and shifting of the neutral axis should be accounted for in design. For stainless steel equal-leg angle columns with Class 4 cross-sections, the following two sets of equations for the design of stainless steel beam-columns—provided respectively in Clause 6.1.9 of EN 1993-1-3 and Clause 5.5 of EN 1993-1-4—take into account interaction between compressive axial load and uniaxial bending moment induced by the effective centroid shifts along the axis of symmetry (major-principal axis) upon local cross-section buckling:

$$\frac{N_{\text{Ed}}}{A_{\text{eff}} f_y / \gamma_{\text{M0}}} + \frac{N_{\text{Ed}} e_{\text{Nv}}}{W_{\text{eff,v,min}} f_y / \gamma_{\text{M0}}} \leq 1.0 \quad (5)$$

$$\frac{N_{\text{Ed}}}{(N_{\text{b,Rd}})_{\text{min}}} + k_v \left( \frac{N_{\text{Ed}} e_{\text{Nv}}}{W_{\text{eff,v}} f_y / \gamma_{\text{M1}}} \right) \leq 1.0 \quad (6)$$

where  $N_{\text{Ed}}$  is the applied design value of the axial compression load;  $e_{\text{Nv}}$  is the effective centroid shift along the major-principal axis when the cross-section is subjected to uniform compression;  $A_{\text{eff}}$  is the effective area

of the cross-section when subjected to uniform compression;  $W_{\text{eff},v}$  is the effective section modulus for the minor principal axis  $v$ - $v$ ;  $(N_{b,Rd})_{\min}$  is the smallest value of the design buckling load  $N_{b,Rd}$  for the following four buckling modes: FB about the major axis  $u$ - $u$ , FB about the minor axis  $v$ - $v$ , torsional buckling (TB) and TFB. The interaction factor  $k_v$  can be obtained as follows:

$$k_v = 1.0 + 2(\bar{\lambda}_v - 0.5) \frac{N_{Ed}}{(N_{b,Rd})_{\min1}} \quad \text{but} \quad 1.2 \leq k_v \leq 1.2 + 2 \frac{N_{Ed}}{(N_{b,Rd})_{\min1}} \quad (7)$$

where  $(N_{b,Rd})_{\min1}$  is the smallest value of  $N_{b,Rd}$  for the following three buckling modes: FB about the minor axis  $v$ - $v$ , TB and TFB.

It should be emphasized here that the design procedure currently prescribed in Eurocode 3 is based on a couple of conceptual flaws that severely influence its performance in predicting the failure loads of equal-leg angle columns buckling in flexural-torsional modes: it does not account for the interaction between flexural-torsional and minor-axis flexural buckling (all columns) and views local buckling and flexural-torsional buckling as two different phenomena, failing to recognize that the former does not occur in angle columns and basically considering the same instability effect twice (class 4 columns). This issue was recently addressed by Behzadi-Sofiani et al. [38], in the context of fixed-ended hot-rolled carbon steel equal-leg angle columns. These authors also demonstrate, analytically, that, in equal-leg angle columns, torsional and local buckling are essentially two designations of the same phenomenon, thus confirming the numerical evidence reported in [39], where it is shown that torsional/local buckling can only occur in longitudinally restrained equal-leg angle columns.

## 5.2. AISC Design Guide 27

In line with the design procedure set out in ANSI/AISC360-10 Specification for Structural Steel Buildings [22], the AISC Design Guide 27 [16] recommends one buckling curve for the design of axially compressed members, which applies to all cross-section types and buckling axes. In accordance with Clause 5.5 of AISC 27 [16], the nominal compressive strength of stainless steel equal-leg angle columns, which is based on the lowest value obtained for FB, TB, and TFB, is calculated from Eq. (8):

$$P_n = F_{cr} A_g \quad (8)$$

where  $A_g$  is the gross cross-sectional area and  $F_{cr}$  is the critical stress determined as

$$F_{cr} = Q \left( 0.50 \frac{Q F_y}{F_e} \right) F_y \quad \text{for} \quad \frac{KL}{r} \leq 3.77 \sqrt{\frac{E}{Q F_y}} \quad (9)$$

$$F_{cr} = 0.531 F_e \quad \text{for} \quad \frac{KL}{r} > 3.77 \sqrt{\frac{E}{Q F_y}} \quad (10)$$

where  $F_e$  is the elastic buckling stress, calculated using Equations (E3-4) and (E4-3), provided in AISC 360 [22], for columns undergoing FB and TB or FTB, respectively;  $Q$  is the reduction factor for local buckling (LB) — for slender unstiffened cross-sections,  $Q = Q_s$ , where  $Q_s$  is calculated in accordance with Clause 5.6.1, AISC 27 [16], whereas  $Q = 1.0$  for non-slender cross-sections;  $F_y$  is the yield stress;  $KL$  is the effective column length and  $r$  is the radius of gyration. The provisions related to TB and FTB checks are required for single angles with  $b / t > 20$ , where  $b$  is the angle leg width and  $t$  is the leg thickness. In accordance with Clause 8.1.1 of AISC 27 [16], the interaction between global minor-axis FB or FTB and the minor-axis bending—caused by effective centroid shifts for slender angle sections—can be checked using the interaction equations provided in Clause H1.1 of AISC 360 [22] intended for checking the doubly and singly symmetric members subjected to flexure and compression:

$$\frac{P_r}{P_c} + \frac{8}{9} \frac{M_{r,v}}{M_{c,v}} \leq 1.0 \quad \text{for} \quad \frac{P_r}{P_c} \geq 0.2 \quad (11)$$

$$\frac{P_r}{2P_c} + \frac{M_{r,v}}{M_{c,v}} \leq 1.0 \quad \text{for} \quad \frac{P_r}{P_c} < 0.2 \quad (12)$$

where  $P_r$  is the applied design value of the axial compression load;  $M_{r,v} = P_r \cdot \Delta e_{Nv}$  is the minor-axis bending caused by effective centroid shifts  $\Delta e_{Nv}$ ;  $P_c$  is the design ( $= P_n \cdot \phi_c$ ) or allowable ( $= P_n / \Omega_c$ ) axial compressive strength where  $\phi_c$  and  $\Omega_c$  are the resistance and compression safety factors, respectively;  $M_{c,v}$  is design ( $= M_{n,v} \cdot \phi_b$ ) or allowable ( $= M_{n,v} / \Omega_b$ ) flexural strength about the minor-principal axis, where  $\phi_b$  and  $\Omega_b$  are the resistance and flexure safety factors, respectively. Note that AISC 27 [16] does not give any explicit recommendation for angle members under flexure. Thus, the nominal flexural strength  $M_{n,v}$  may be determined according to Clause F.10 of AISC 360 [22]: for equal-leg angle sections subjected to flexure about the minor-principal axis, the nominal flexural strength  $M_n$  is the yield cross-section bending strength about the minor-principal axis for non-slender sections, whereas in the case of slender angle sections, it is the cross-section bending strength for leg local buckling. However, it is important to note that the limiting value of width-to-thickness ratios for legs of axially compressed angle columns stated in Table 3-1 of AISC 27 [16] for stainless steel, and Table B4.1a of AISC 360 [22] for carbon steel, are not the same. Furthermore,

whereas AISC 360 [22] offers the limiting value of the width-to-thickness ratio for legs of angle members subject to flexure in Table B4.1a, the equivalent value for stainless steel angles is not provided in Table 3-2 of AISC 27 [16]. Hence, the absence of explicit recommendations for stainless steel angle members subjected to the interaction of compression load and bending in AISC 27 [16] can lead to result inaccuracy in the design practice.

### **5.3. Accuracy assessment of the design procedures for equal-leg angle columns provided in European and AISC specifications**

In this subsection, the accuracy of the European and AISC design methods for the buckling strength predictions of equal-leg angle columns, described in the previous subsections, is investigated with respect to hot-rolled and laser-welded angles produced from austenitic stainless steel alloy. The FE data obtained through the parametric study presented in Section 4 and the experimental data, related to stub column tests and global buckling tests collected from literature [2], [3], [12], [13], [14], [15], [18], [19] are utilised in the comparative study. The FE failure modes governed by FTB (local similar-section deformations with predominantly torsional features) of very short length columns, major-axis FTB or minor-axis FB of short, intermediate and large length columns were carefully considered and analysed to evaluate the corresponding design failure loads. The procedure described in Clause 5.2.3, EN 1993-1-4 [1] was followed to obtain the effective areas of the slender angle sections (Class 4). For consistency with the local buckling curve for outstand elements, the slenderness limit for Class 3 was used as  $b/t = 14\varepsilon$  as is stated in Table 5.2, EN 1993-1-4 [1], where  $b$  and  $t$  are the leg width and thickness respectively, and  $\varepsilon$  is the material coefficient. Unlike Eurocode 3 procedures, the effects caused by the loss of full cross-section effectiveness due to local buckling are implicitly included in design methods given in AISC specifications. To evaluate the influence of the bending moment caused by the shift in neutral axis due to the local buckling, the data points related to slender cross-sections were selected and reassessed based on interaction formulae stated in Clause 5.5 [1] and Clause H1.1 [22], respectively. The neutral axis shifted towards the angle heel along the major-principal axis causes a secondary minor-axis bending moment with no secondary major axis bending moment (bending towards the angle heel). The effective centroid shift was determined as the distance between centroids of a full, unreduced and effective equal-leg angle section. For cases in which FTB was the critical mode, the



accuracy assessment included two approaches: (i) the use of the effective cross-sectional area for columns with slender, Class 4 angle-sections and the use of gross cross-sectional areas for all other columns with non-slender cross-sections, and (ii) the use of gross cross-sectional areas for all column capacity calculations, to avoid double-accounting of the local/torsional buckling.

The safety factors were taken as equal to 1.0 in the predictions of the ultimate column resistances on the basis of each design methods (i.e.  $\gamma_{M1} = 1.0$  and  $\phi_c = \Omega_c = 1.0$ ).

Graphical evaluations were performed, with the results displayed in Fig. 16 and Fig. 17 where the European buckling curves  $b$  ( $\alpha = 0.34$ ),  $c$  ( $\alpha = 0.49$ ) and  $d$  ( $\alpha = 0.76$ ) in conjunction with a limiting non-dimensional slenderness  $\bar{\lambda}_0 = 0.2$ , and AISC 27 curve (for non-slender angle-sections) are compared with the FE and test ultimate loads normalised by the cross-section yield loads, with respect to minor-axis FB of HRSS and LWSS equal-leg angle columns, respectively. The FE and test ultimate loads for very short columns normalised with cross-section yield loads are also included in these graphs. The data points are plotted against the non-dimensional minor-axis FB column slenderness ratio  $\bar{\lambda}_v$ . In addition, Fig. 18 and Fig. 19 compare the FE and test normalised column resistances, plotted against the flexural-torsional (FT) column slenderness ratio  $\bar{\lambda}_{FT}$ , with Eurocode and AISC buckling curves for major-axis FTB of HRSS and LWSS equal-leg angle columns, respectively. The accuracy of Eurocode design procedures for buckling curves  $c$  and  $d$  is also shown in Fig. 20 and Fig. 21 where the data points, representing pairs of corresponding FE and test data ( $N_{b,u}$ ), and design data ( $N_{b,u,pred}$ ) related to minor-axis FB, are respectively plotted for HRSS and LWSS angle columns, including both slender and non-slender cross-sections, whereas Fig. 22 compares the accuracy of AISC procedures used for design of HRSS and LWSS angle columns. In addition, Fig. 23 presents comparisons between FE and test data  $N_{b,u}$ , and design data  $N_{b,u,pred}$  calculated using codified design procedures for FTB, considering both HRSS and LWSS angle columns and including slender and non-slender angle sections. The gross cross-sectional areas were used here for all FTB column capacity calculations.

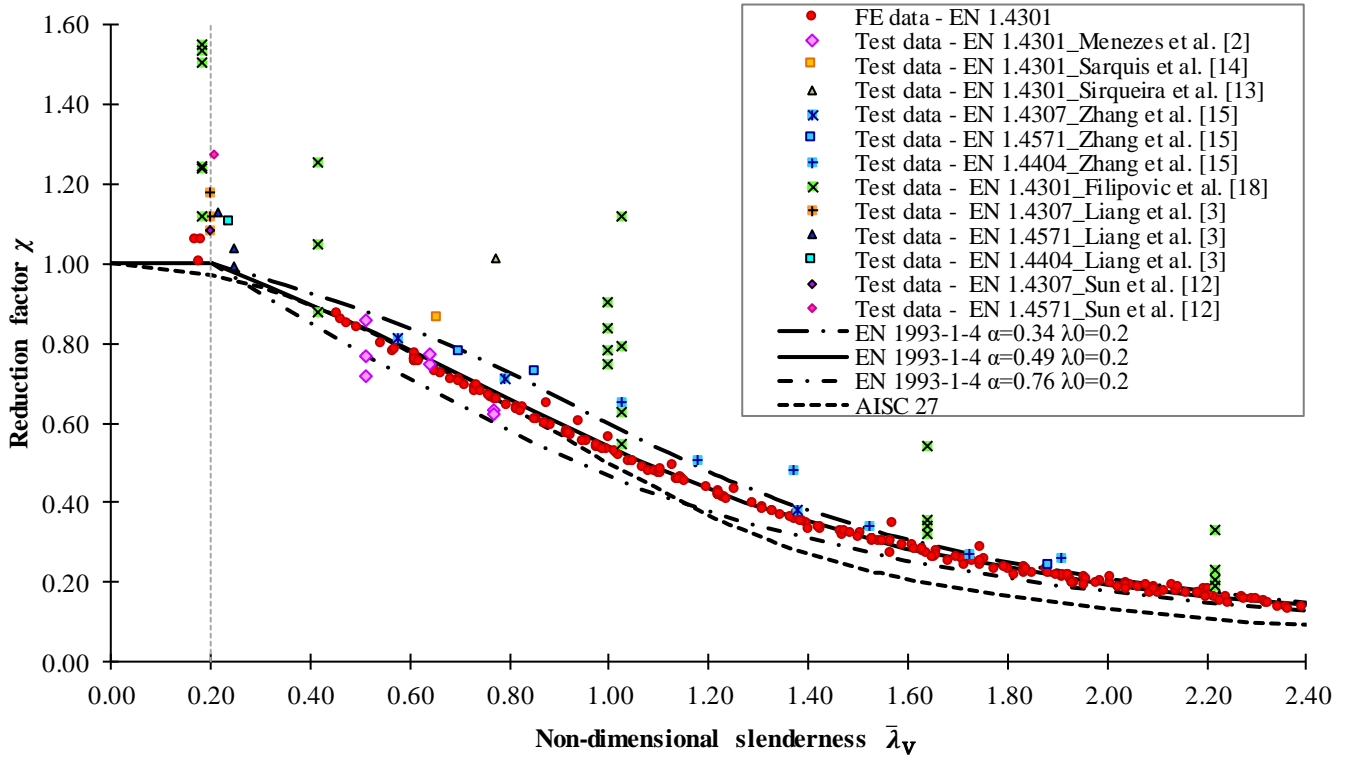


**Fig. 16** Comparison of normalised FE and test data against those obtained using EN 1993-1-4 and AISC 27 for minor-axis FB of HRSS angle columns.

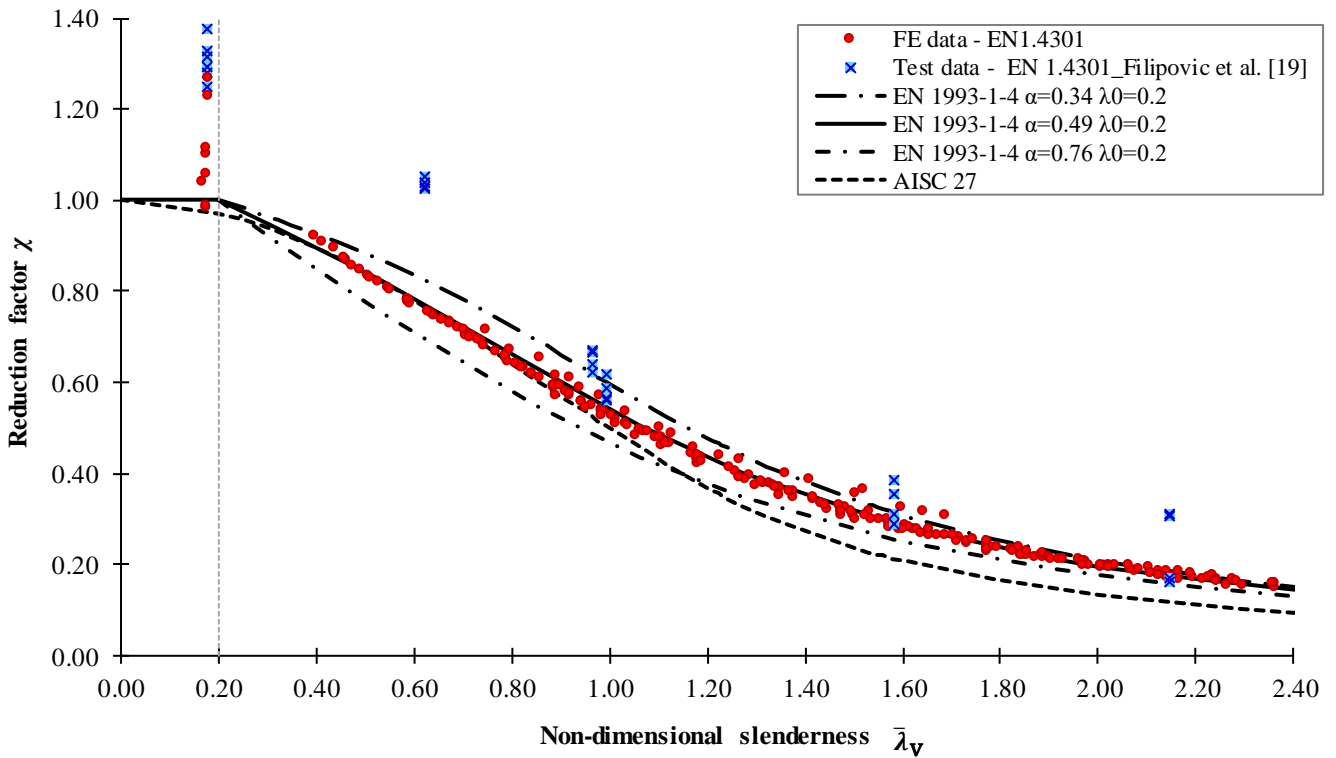


**Fig. 17** Comparison of normalised FE and test data against those obtained using EN 1993-1-4 and AISC 27 for minor-axis FB of LWSS angle columns.

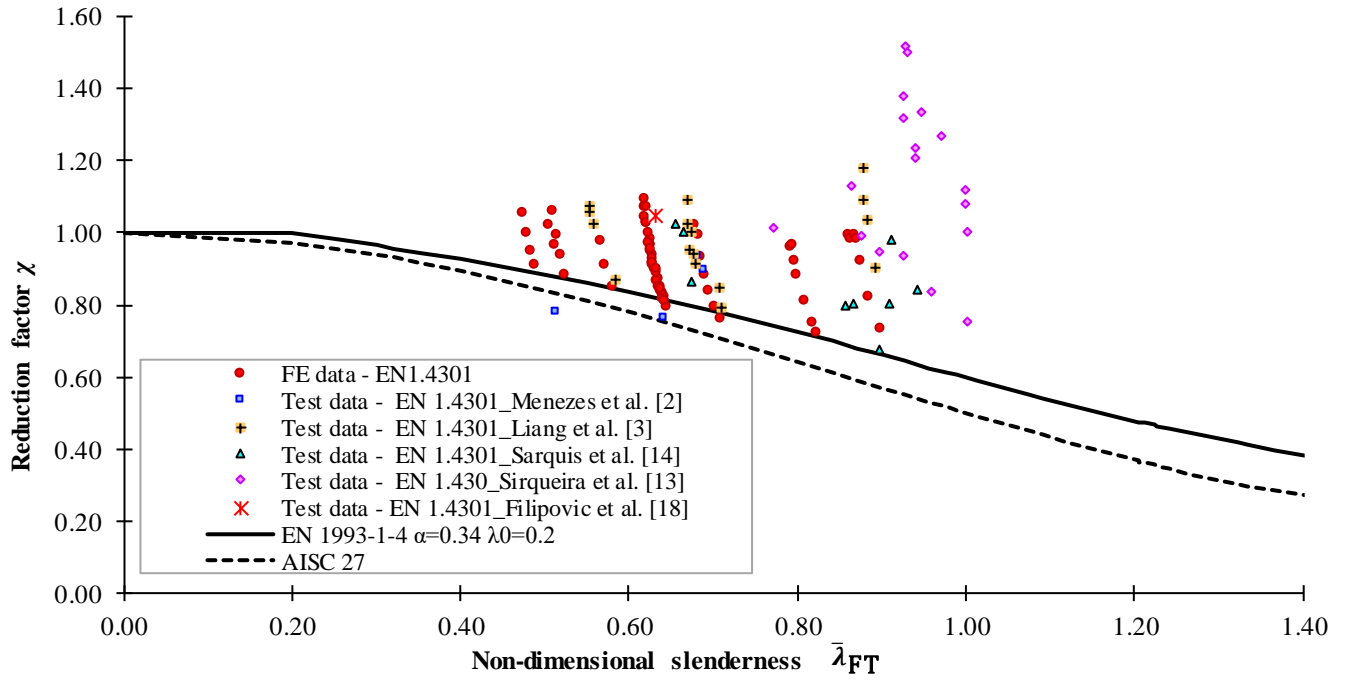


**Fig. 18** Comparison of normalised FE and test data against those obtained using EN 1993-1-4 and AISC 27 for FTB of HRSS angle columns.

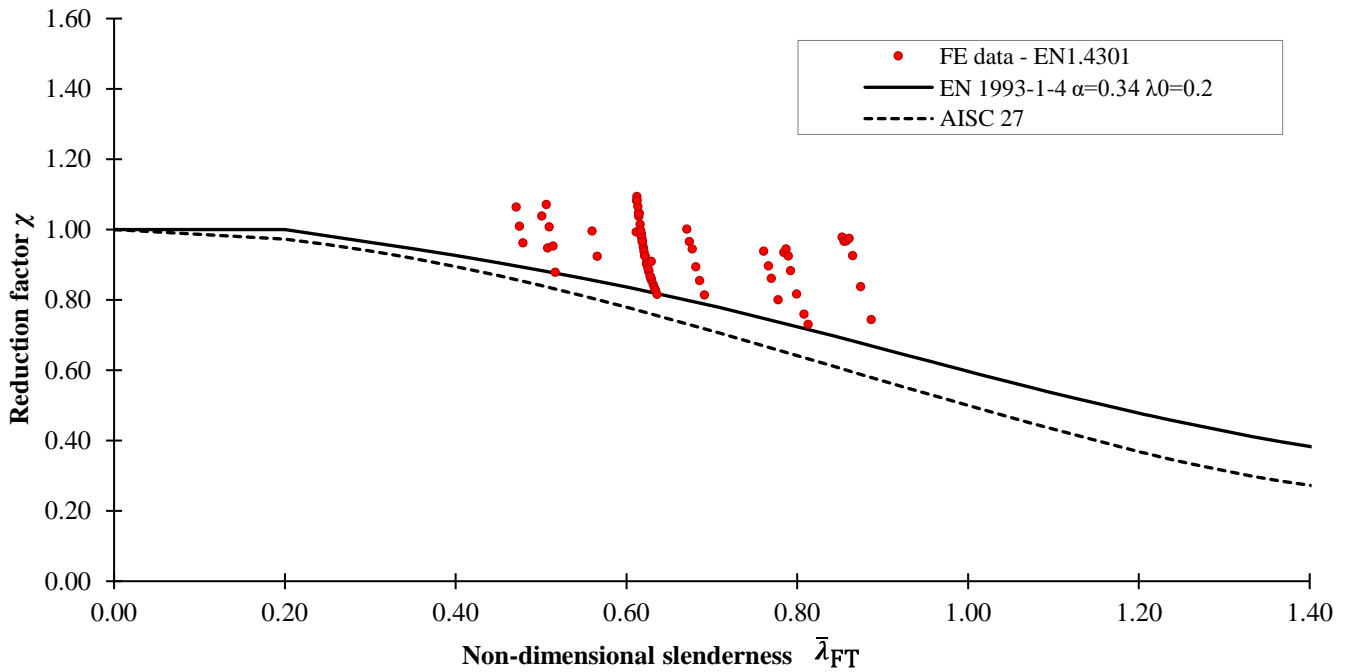
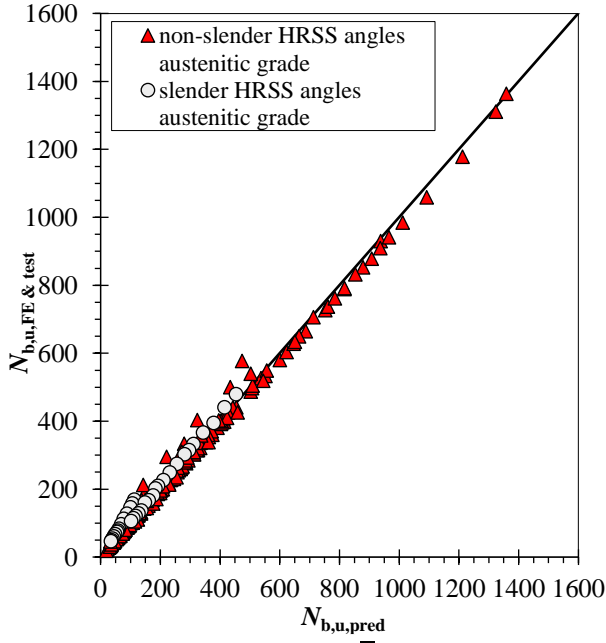
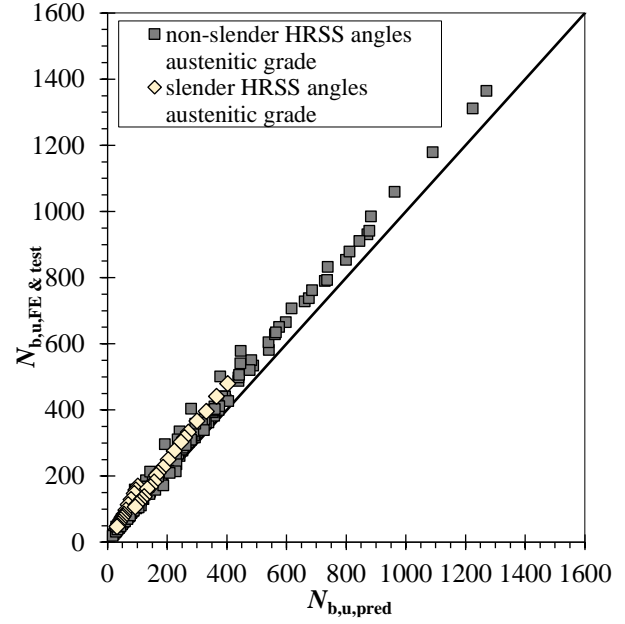


**Fig. 19** Comparison of normalised FE and test data against those obtained using EN 1993-1-4 and AISC 27 for FTB of LWSS angle columns.

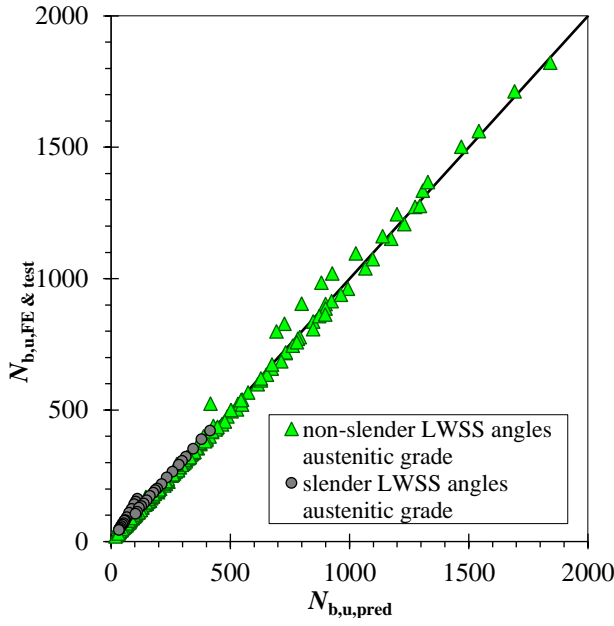


(a) EN 1993-1-4 /  $\alpha = 0.49 \bar{\lambda}_0 = 0.2$  & Eq. (6)

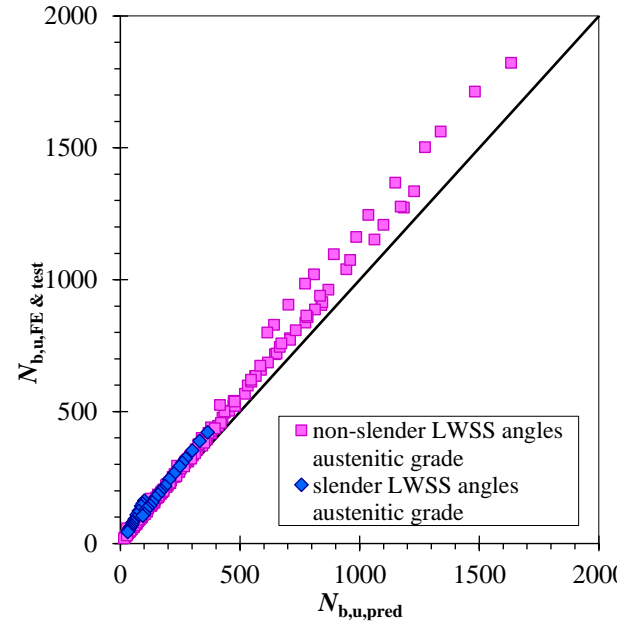


(b) EN 1993-1-4 /  $\alpha = 0.76 \bar{\lambda}_0 = 0.2$  & Eq. (6)

**Fig. 20** Comparison of FE and test data resistance with those obtained using EN 1993-1-4 for minor-axis FB of HRSS angle columns.

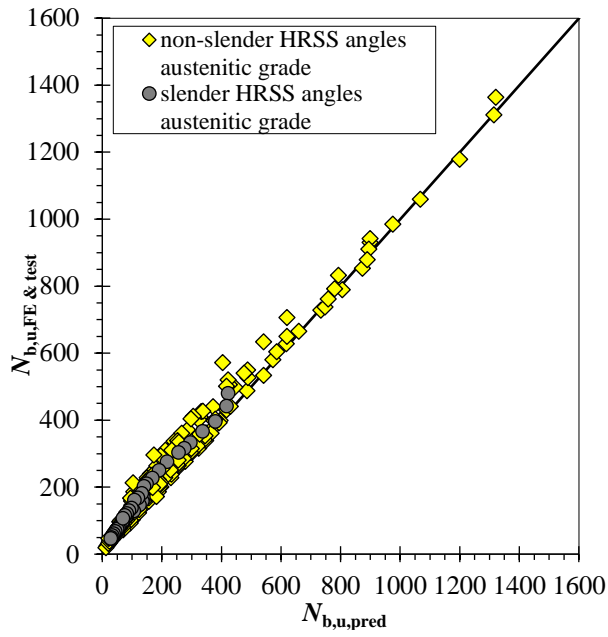


(c) EN 1993-1-4 /  $\alpha = 0.49 \bar{\lambda}_0 = 0.2$  & Eq. (6)

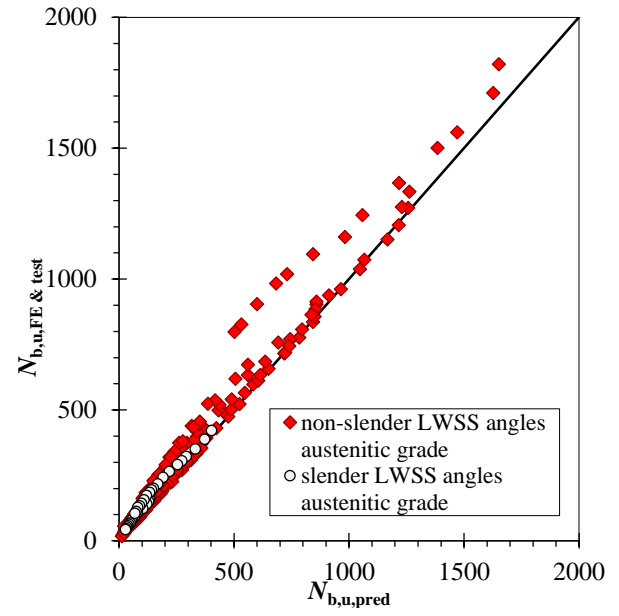


(d) EN 1993-1-4 /  $\alpha = 0.76 \bar{\lambda}_0 = 0.2$  & Eq. (6)

**Fig. 21** Comparison of FE and test data resistance with those obtained using EN 1993-1-4 for minor-axis FB of LWSS angle columns.

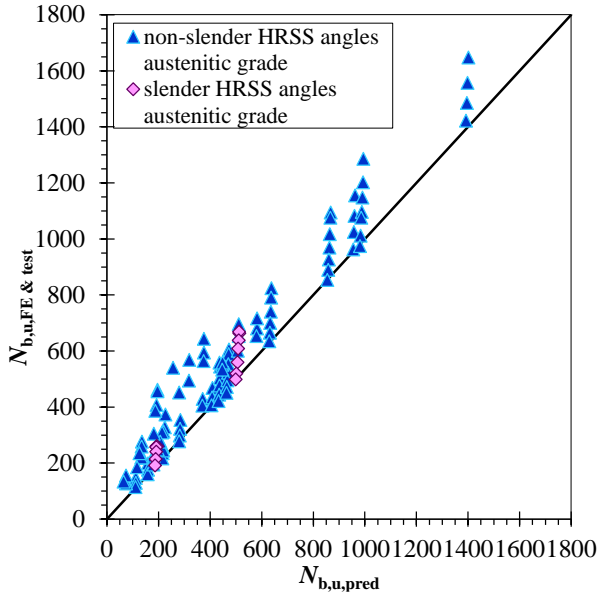


(a) AISC 27 curve & Eqs. (11), (12) / HRSS angle columns

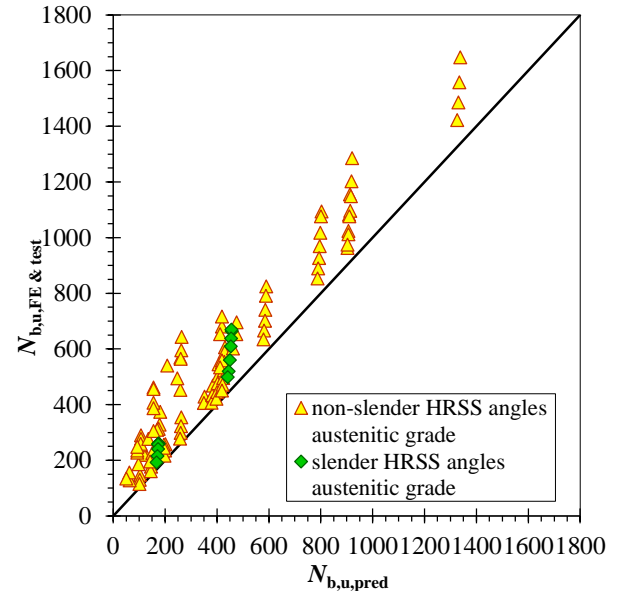


(b) AISC 27 curve & Eqs. (11), (12) / LWSS angle columns

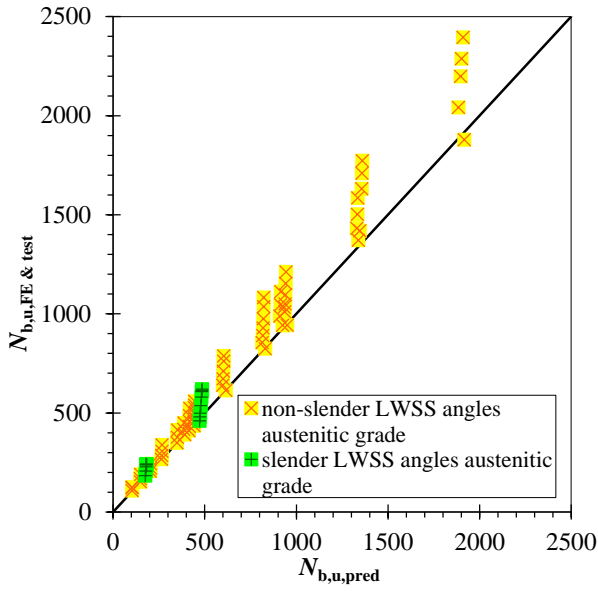
**Fig. 22** Comparison of FE and test data resistance with those obtained using AISC 27 for minor-axis FB of HRSS and LWSS angle columns.



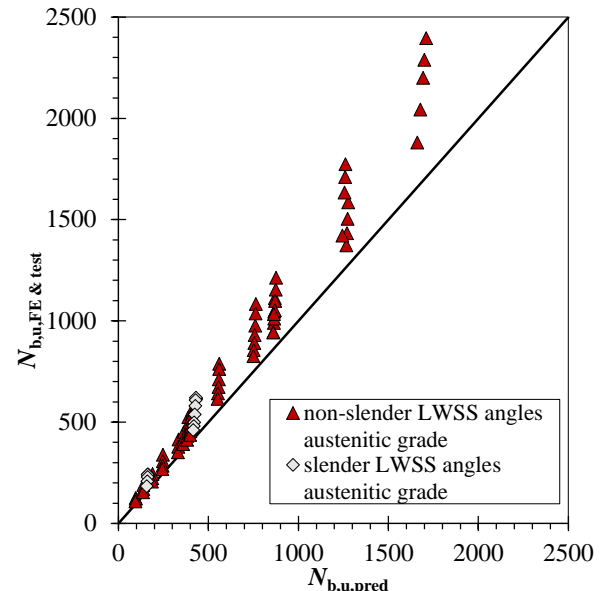
(a) EN 1993-1-4 /  $\alpha = 0.34 \bar{\lambda}_0 = 0.2$  / HRSS angle columns



(b) AISC 27 curve / HRSS angle columns



(a) EN 1993-1-4 /  $\alpha = 0.34 \bar{\lambda}_0 = 0.2$  / LWSS angle columns



(b) AISC 27 curve / LWSS angle columns

**Fig. 23** Comparison of FE and test data resistance with those obtained using EN 1993-1-4 and AISC 27 for major-axis FTB of HRSS and LWSS angle columns.

A statistical appraisal of the accuracy of each codified procedure for the buckling strength predictions of HRSS and LWSS equal-leg angle columns are provided in Table 9 and Table 10, respectively, considering the FE and test-to-predicted ratios  $N_{b,u}/N_{b,u,pred}$ .

**Table 9.** Comparison of FE and test data with design data for HRSS angle columns.

Grade	Cross-section slenderness	Code	Data no.	$N_{b,u}/N_{b,u,pred}$	
			$\bar{\lambda}_0 > 0.2$	Mean	CoV (%)
Austenitic		EN 1993-1-4, EN 1993-1-1 / minor-axis FB (and minor-axis bending)			
	Non-slender	$\alpha = 0.76 \ \bar{\lambda}_0 = 0.2$ & gross cross-sectional area	203	1.134	8.2
	Slender	$\alpha = 0.76 \ \bar{\lambda}_0 = 0.2$ & Eq. (6) & effective cross-sectional area	34	1.351	14.3
	Non-slender	$\alpha = 0.49 \ \bar{\lambda}_0 = 0.2$ & gross cross-sectional area	203	1.009	8.2
	Slender	$\alpha = 0.49 \ \bar{\lambda}_0 = 0.2$ & Eq. (6) & effective cross-sectional area	34	1.213	15.1
EN 1993-1-4 / FTB (and minor-axis bending)					
Austenitic	Non-slender	$\alpha = 0.34 \ \bar{\lambda}_0 = 0.2$ & gross cross-sectional area	100	1.308	25.3
	Slender	$\alpha = 0.34 \ \bar{\lambda}_0 = 0.2$ & Eq. (6) & effective cross-sectional area	14	1.563	22.0
		$\alpha = 0.34 \ \bar{\lambda}_0 = 0.2$ & gross cross-sectional area	14	1.217	10.6
	All data (non-slender & slender)	$\alpha = 0.34 \ \bar{\lambda}_0 = 0.2$ & gross cross-sectional area	114	1.298	24.2
AISC 27 / minor-axis FB (and minor-axis bending)					
Austenitic	Non-slender	AISC 27 curve	203	1.283	17.8
	Slender	AISC 27 curve & Eqs. (11), (12)	34	1.374	13.6
AISC 27 / FTB (and minor-axis bending)					
Austenitic	Non-slender	AISC 27 curve	100	1.553	33.8
	Slender	AISC 27 curve & Eqs. (11), (12)	14	1.522	14.3
		AISC 27 curve	14	1.354	10.1
	All data (non-slender & slender)	AISC 27 curve	114	1.529	32.6

**Table 10.** Comparison of FE and test data with design data for LWSS angle columns.

Grade	Cross-section slenderness	Code	Data no. $\bar{\lambda}_0 > 0.2$	$N_{b,u}/N_{b,u,pred}$	
				Mean	CoV (%)
		EN 1993-1-4, EN 1993-1-1 / minor-axis FB (and minor-axis bending)			
Austenitic	Non-slender	$\alpha = 0.76 \ \bar{\lambda}_0 = 0.2$ & gross cross-sectional area	213	1.129	6.4
	Slender	$\alpha = 0.76 \ \bar{\lambda}_0 = 0.2$ & Eq. (6) & effective cross-sectional area	33	1.310	13.6
	Non-slender	$\alpha = 0.49 \ \bar{\lambda}_0 = 0.2$ & gross cross-sectional area	213	1.001	6.7
	Slender	$\alpha = 0.49 \ \bar{\lambda}_0 = 0.2$ & Eq. (6) & effective cross-sectional area	33	1.173	14.6
		EN 1993-1-4 / FTB (and minor-axis bending)			
Austenitic	Non-slender	$\alpha = 0.34 \ \bar{\lambda}_0 = 0.2$ & gross cross-sectional area	68	1.130	8.2
	Slender	$\alpha = 0.34 \ \bar{\lambda}_0 = 0.2$ & Eq. (6) & effective cross-sectional area	15	1.484	22.1
		$\alpha = 0.34 \ \bar{\lambda}_0 = 0.2$ & gross cross-sectional area	15	1.194	10.5
	All data (non-slender & slender)	$\alpha = 0.34 \ \bar{\lambda}_0 = 0.2$ & gross cross-sectional area	83	1.142	8.9
		AISC 27 / minor-axis FB (and minor-axis bending)			
Austenitic	Non-slender	AISC 27 curve	213	1.262	17.8
	Slender	AISC 27 curve & Eqs. (11), (12)	33	1.351	12.9
		AISC 27 / FTB (and minor-axis bending)			
Austenitic	Non-slender	AISC 27 curve	68	1.222	8.2
	Slender	AISC 27 curve & Eqs. (11), (12)	15	1.474	14.9
		AISC 27 curve	15	1.335	10.0
	All data (non-slender & slender)	AISC 27 curve	83	1.243	9.2

Following the results of the comparative analysis, the following conclusions can be drawn:

- The nominal geometries — cross-section dimensions and lengths of the HRSS and LWSS angle specimens, reported in Table 2 and Table 3, were chosen to be the same, enabling direct comparisons between key experimental results obtained through buckling tests [18], [19]. By comparing experimental data in these tables, it can be seen that the ultimate compressive capacities of the tested HRSS angle columns are higher than those obtained in the case of equivalent LWSS angle columns, for both stub-column tests and global buckling tests.
- The cross-sections of both HRSS and LWSS angle columns are less sensitive to elastic buckling; the largest number of analysed cross-sections underwent yielding and strain hardening before inelastic (plastic) buckling was reached. For austenitic grade EN 1.4301, the Eurocode design procedure, based on the effective width method, gives the same predictions of the cross-section instability modes as FE modelling.
- In the very low slenderness range, the data trend exhibits that plateau length with the limiting non-dimensional slenderness of  $\bar{\lambda}_0 = 0.2$  is suitable for developing design buckling curves for both HRSS and LWSS equal-leg angle columns.
- Fig. 16 and Fig. 17 reveal a relatively good agreement between FE data and Eurocode buckling curve *c* ( $\alpha = 0.49$ ,  $\bar{\lambda}_0 = 0.2$ ) [21] for minor-axis FB of HRSS and LWSS angle columns, respectively. However, the results of the graphical evaluations also indicate that this buckling curve results in a certain level of unsafe predictions of FB strengths for the dataset in the intermediate slenderness range with non-dimensional column slenderness  $\bar{\lambda}_v$  between 0.5 and 1.0. Concerning that the considered Eurocode 3 buckling curves were initially developed for carbon steel columns, the discrepancy of FE and test data from design predictions in this slenderness area can be explained by the influences of higher residual stress magnitudes and the material non-linearity (the nonlinear material softening between the proportionality stress and the yield stress) in the case of stainless steel columns.



- Comparisons of FE and test minor-axis FB resistances with those calculated by using buckling curve  $d$  ( $\alpha = 0.76$ ,  $\bar{\lambda}_0 = 0.2$ ) [21], demonstrate that this curve is generally conservative both for slender and non-slender HRSS and LWSS angle sections, see Fig. 20b and Fig. 21b.
- The design procedure including interaction of axial compression and uniaxial minor-axis moment for columns with slender angle sections, failed by minor-axis FB, gives acceptable and safe results but with noticeable data scatter, considering both buckling curves  $c$  and  $d$  [21], as it is reported in Table 9 and Table 10.
- The AISC 27 [16] codified procedure for stainless steel angle columns provides overly conservative and scattered predictions of minor-axis FB strength for HRSS and LWSS equal-leg angle columns, including both slender and non-slender sections (see Fig. 20c and Fig. 21c). As can be seen from Fig. 16 and Fig. 17, the AISC 27 design buckling curve results in more accurate minor-axis FB strength predictions in the intermediate slenderness range up to approximately  $\bar{\lambda}_v = 1.0$ , but offers much more conservative predictions for the dataset in the high slenderness range; thus, the conservatism of the AISC 27 minor-axis FB strength predictions increases with the increasing column slenderness.
- The governing failure of HRSS and LWSS equal-leg angle columns in the low and partially in the intermediate slenderness range is major-axis FTB. When buckling curve  $b$  ( $\alpha = 0.34$ ,  $\bar{\lambda}_0 = 0.2$ ) [1] is used for buckling resistance check, the FE and test dataset show a high degree of scatter with highly conservative distributions. A similar data trend was also found in the case of AISC 27 design criteria for FTB resistances. However, when gross cross-sectional areas were used to calculate the FTB resistances of columns with slender sections, a lower level of conservatism and data scatter can be seen in Table 9 and Table 10. The scattering of the included experimental data related to HRSS columns failing by FTB, which is missing in the case of LWSS angle columns, contributes to higher data scatter in the case of HRSS columns with non-slender angle sections ( see Table 9 and Table 10).

## 6. Reliability assessment

In this section, the reliability of the proposed Eurocode buckling curves for design HRSS and LWSS equal-leg angle columns is assessed through the procedure outlined in Annex D of EN 1990 [40], utilising the FE

data from the parametric studies performed in Section 4 and the collected experimental data [2], [3], [12], [13], [14], [15], [18], [19]. In accordance with the provisions stated in Clause D8.2.2.5 [40], the total database was divided into sub-sets, depending on the group of data being considered, i.e. minor-axis FB, major-axis FTB or their interaction with uniaxial minor-axis bending and cross-section slenderness (non-slender and slender sections). The described methodology allows the total data point number to be used in the original series to assess the fractile factor avoiding large safety factors due to a smaller number of data points in each sub-set.

In the present reliability analyses, the material over-strength factor for austenitic stainless steel was taken as 1.3 with a CoV of 6%, whereas the CoV of the variability of the geometric properties was taken equal to 5%, as recommended by Afshan et al. [41].

The key statistical parameters of the reliability analysis are summarised in Table 11 and Table 12 for HRSS and LWSS equal-leg angle columns, respectively. In total, 351 FE and test data points were considered for HRSS angle columns, whereas for LWSS angle columns, this number was 329. In Table 11 and Table 12,  $n$  is the number of FE data and test data taken into consideration;  $b$  is the average ratio of FE and test-to-model resistance based on a least squares fit to all the data;  $V_\delta$  is the coefficient of variation of the FE and test data relative to the resistance model, and  $\gamma_{M1}$  is the partial safety factor for the buckling resistance.

**Table 11.** Reliability analysis of the proposed design criteria for HRSS equal-leg angle columns.

Grade	Cross-section slenderness	Code	Dataset	$n$ ( $\bar{\lambda} > \bar{\lambda}_0$ )	$b$	$V_\delta$	$\gamma_{M1}$
EN 1993-1-4, EN 1993-1-1 / minor-axis FB (and minor-axis bending)							
Austenitic	Non-slender	$\alpha = 0.76$ $\bar{\lambda}_0 = 0.2$ & gross cross-sectional area	FE and test data	203	1.160	0.057	0.99
			Test data only	22	1.251	0.053	0.84
	Slender	$\alpha = 0.76$ $\bar{\lambda}_0 = 0.2$ & Eq. (6) & effective cross-sectional area	FE data only	34	1.230	0.053	0.93
			Test data only	-	-	-	-
	Non-slender	$\alpha = 0.49$ $\bar{\lambda}_0 = 0.2$ & gross cross-sectional area	FE and test data	203	0.988	0.055	1.10
			Test data only	22	1.134	0.045	0.91
	Slender	$\alpha = 0.49$ $\bar{\lambda}_0 = 0.2$ & Eq. (6) & effective cross-sectional area	FE data only	34	1.087	0.057	1.06
			Test data only	-	-	-	-
EN 1993-1-4 / FTB (and minor-axis bending)							
Austenitic	Non-slender	$\alpha = 0.34$ $\bar{\lambda}_0 = 0.2$ & gross cross-sectional area	FE and test data	100	1.147	0.125	1.10
			Test data only	42	1.371	0.084	1.12
			FE data only	14	1.310	0.052	0.85
	Slender	$\alpha = 0.34$ $\bar{\lambda}_0 = 0.2$ & gross cross-sectional area	FE data only	14	1.185	0.021	0.93
			Test data only	-	-	-	-
	All data (non-slender & slender)	$\alpha = 0.34$ $\bar{\lambda}_0 = 0.2$ & gross cross-sectional area	FE and test data	114	1.150	0.126	1.10
			Test data only	-	-	-	-

**Table 12.** Reliability analysis of the proposed design criteria for LWSS equal-leg angle columns.

Grade	Cross-section slenderness	Code	Dataset	$n \left( \bar{\lambda} > \bar{\lambda}_0 \right)$	$b$	$V_\delta$	$\gamma_{M1}$
EN 1993-1-4, EN 1993-1-1 / minor-axis FB (and minor-axis bending)							
Austenitic	Non-slender	$\alpha = 0.76 \quad \bar{\lambda}_0 = 0.2$ & gross cross-sectional area	FE and test data	213	1.132	0.048	0.96
			Test data only	5	1.259	0.084	0.90
	Slender	$\alpha = 0.76 \quad \bar{\lambda}_0 = 0.2$ & Eq. (6) & effective cross-sectional area	FE data only	33	1.193	0.048	0.96
			Test data only	-	-	-	-
	Non-slender	$\alpha = 0.49 \quad \bar{\lambda}_0 = 0.2$ & gross cross-sectional area	FE and test data	213	1.002	0.045	1.08
			Test data only	5	1.196	0.084	0.95
	Slender	$\alpha = 0.49 \quad \bar{\lambda}_0 = 0.2$ & Eq. (6) & effective cross-sectional area	FE data only	33	1.048	0.053	1.10
			Test data only	-	-	-	-
EN 1993-1-4 / FTB (and minor-axis bending)							
Austenitic	Non-slender	$\alpha = 0.34 \quad \bar{\lambda}_0 = 0.2$ & gross cross-sectional area	FE data only	68	1.141	0.038	0.90
			Test data only	-	-	-	-
			$\alpha = 0.34 \quad \bar{\lambda}_0 = 0.2$ & Eq. (6) & effective cross-sectional area	FE data only	15	1.232	0.058
	Slender	$\alpha = 0.34 \quad \bar{\lambda}_0 = 0.2$ & gross cross-sectional area	FE data only	15	1.158	0.023	0.93
			Test data only	-	-	-	-
	All data (non-slender & slender)	$\alpha = 0.34 \quad \bar{\lambda}_0 = 0.2$ & gross cross-sectional area	FE data only	83	1.141	0.045	0.91
			Test data only	-	-	-	-

Based on the results of the reliability analysis, the following comments can be drawn:

- The assessment of European codified procedures shows that the buckling curve  $c$  ( $\alpha = 0.49, \bar{\lambda}_0 = 0.20$ ) [21] can be safely adopted for the design of both for HRSS and LWSS equal-leg angle columns, produced from austenitic grade and susceptible to minor-axis FB, considering both non-slender and slender angle sections.
- The buckling curve  $d$  ( $\alpha = 0.76, \bar{\lambda}_0 = 0.20$ ) [21] leads to safe but quite conservative ultimate strength predictions with partial safety factors noticeably lower than the partial safety factor value of  $\gamma_{M1} = 1.10$  recommended in EN 1993-1-4 [1], both for HRSS and LWSS equal-leg angle columns undergoing minor-axis FB.
- The reliability analyses show that the current design method stated in EN 1993-1-4 [1] intended for checking column stability against FTB, provides safe predictions with the resistance factors  $\gamma_{M1}$  lower than 1.10 both for HRSS and LWSS equal-leg angle columns, when both test and FE data are considered. When only the available test data are considered (only for HRSS columns with non-slender angle sections), the partial safety factor  $\gamma_{M1}$  is higher than 1.10; this is due to the variation and

scattering of the test data obtained from different experiments collected from literature [2], [3], [12], [13] [14], and [18].

## 7. Conclusions

The minor-axis FB and major-axis FTB behaviour and design of compressed pin-ended austenitic stainless steel equal-leg angle columns, manufactured by hot-rolling and laser-welding processes, were investigated in this study. Advanced and realistic FE modelling, able to replicate their structural responses, were performed and validated against experimental results from the literature. Based on FE modelling, extensive numerical parametric studies were carried out. Both slender and non-slender sections were examined over a wide range of column slenderness values. The generated data, together with experimental data from the literature [2], [3], [12], [13], [14], [15], [18], [19] were then compared with the current European EN 1993-1-4 [1] and AISC Design Guide 27 [16] design methods. The appropriateness of the different codified buckling curves (considering the shift of the centroid for Class 4 cross-sections) was evaluated. A reliability assessment was undertaken for the European codified procedure according to the methodology proposed in Annex D, EN 1990:2002 [40] and research of Afshan et al. [41].

Based on the obtained results we conclude the following:

- For minor-axis FB, the buckling curve  $c$  ( $\alpha = 0.49$ ) in conjunction with the non-dimensional limiting slenderness  $\bar{\lambda}_0 = 0.2$  may be safely used for the design of hot-rolled and laser-welded austenitic stainless steel columns both for non-slender and slender cross-sections. The safety factors  $\gamma_{M1}$  are equal to or lower than 1.10.
- The buckling curve  $d$  ( $\alpha = 0.76$ ) in conjunction with the non-dimensional limiting slenderness  $\bar{\lambda}_0 = 0.2$  offers safe but more conservative predictions of minor-axis FB strengths both for hot-rolled and laser-welded austenitic stainless steel columns, in comparison with buckling curve  $c$ . The accuracy assessment also indicated lower scattering when slender angle sections are considered. The safety factors  $\gamma_{M1}$  are equal to 0.99 and 0.84 for non-slender and slender cross-sections, respectively for hot-rolled stainless steel angle columns, whereas the safety factor  $\gamma_{M1}$  is equal to 0.96 both for non-slender and slender sections, respectively, for laser-welded stainless steel angle columns.

- The use of buckling curve  $b$  ( $\alpha = 0.34$ ) in conjunction with  $\bar{\lambda}_0 = 0.2$  to predict FTB leads to safe but quite conservative results characterized by significantly higher scatter and safety factors equal to or lower than 1.10, when both experimental and numerical data are considered. An exception was found for HRSS angle columns when only the experimental dataset is included in the analysis; in that case, the safety factor  $\gamma_{M1}$  is equal to 1.12. It is proposed that the gross cross-sectional area be used for all classes of column cross-sections in design predictions of FTB modes.
- A comparison of the results with the current AISC Design Guide 27 [16] indicates that the codified procedures for column design lead to overly conservative and scattered predictions of minor-axis FB and FTB strengths for hot-rolled and laser-welded stainless steel angle columns, including both slender and non-slender cross-sections, thereby demonstrating a considerable need for their improvement.

## Funding

This investigation is supported by the Serbian Ministry of Education, Science and Technological Development through the 200092 project.

**Declarations of interest:** none

## Acknowledgements

The authors are grateful to companies Montanstahl ag Switzerland, Vetroelektrane Balkana Belgrade, Armont SP Belgrade, Institute for Testing of Materials Belgrade, Institute for Materials and Structures Faculty of Civil Engineering University of Belgrade, ConPro Novi Sad, Energoprojekt Industrija PLC Belgrade, Vekom Geo Belgrade, CO-Designing, Peri Oplate Belgrade, North Engineering Subotica, Amiga Kraljevo, Mašinoprojekt kopriv PLC Belgrade, Sika Belgrade, DvaD Solutions Belgrade and Soko Inžinering Belgrade for their support.

## References

- [1] Eurocode 3: Design of steel structures – part 1-4: General rules – supplementary rules for stainless steels, including amendment A1 (2015), EN 1993-1-4:2006+A1:2015, CEN, Brussels (Belgium), 2015.

- [2] A.A. de Menezes, P.C.G. Pedro, L.R.O. de Lima, A.T. da Silva, Experimental and numerical investigation of austenitic stainless steel hot-rolled angles under compression, *Journal of Constructional Steel Research* 152 (2019) 42–56.
- [3] Y. Liang, V.V.K Jeyapragasam, L. Zhang, O. Zhao, Flexural-torsional buckling behaviour of fixed-ended hot-rolled austenitic stainless steel equal-leg angle section columns, *Journal of Constructional Steel Research* 154 (2019) 43–54.
- [4] SEI/ASCE 8-02: Specification for the Design of Cold-Formed Stainless Steel Structural Members, American Society of Civil Engineers, 2003.
- [5] AS/NZS 4673:2001: Cold-formed stainless steel structures. Australian – New Zealand Standard, Standards Australia, 2001.
- [6] P.B. Dinis, D. Camotim, A novel DSM-based approach for the rational design of fixed ended and pin-ended short-to-intermediate thin-walled angle columns, *Thin-Walled Structures* 87 (2015) 158–182.
- [7] Z. Wang, Y. Wang, X. Yun, L. Gardner, X. Hu, Experimental and Numerical Study of Fixed-Ended High-Strength Aluminum Alloy Angle-Section Columns, *Journal of Structural Engineering* 146 (10) (2020).
- [8] Eurocode 9: Design of aluminum structures—Part 1-1: General rules and rules for buildings. EN 1999-1-1, CEN Brussels (Belgium), 2007.
- [9] Code for design of aluminium structures (In Chinese) GB 50429-2007, MOHURD (Ministry of Housing and Urban-Rural Development of the People’s Republic of China), Beijing, 2007.
- [10] Aluminum design manual, AA (Aluminum Association), Washington, (2010).
- [11] P. B.Dinis and D. Camotim, Proposal to improve the DSM design of cold-formed steel angle columns: Need, background, quality assessment, and illustration, *Journal of Structural Engineering* 145 (8) (2019).
- [12] Y. Sun, Z. Liu, Y. Liang, O. Zhao, Experimental and numerical investigations of hot-rolled austenitic stainless steel equal-leg angle sections, *Thin-Walled Structures* 144 (2019) 1–12.

- [13] A. da S. Sirqueira, P.C.G. da S. Vellasco, L.R.O. de Lima, F.R. Sarquis, Experimental assessment of stainless steel hot-rolled equal legs angles in compression, *Journal of Constructional Steel Research* 169 (2020).
- [14] F.R. Sarquis, L.R.O. de Lima, P.C.G. da S. Vellasco, M.C. Rodrigues, Experimental and numerical investigation of hot-rolled stainless steel equal leg angles under compression, *Thin-Walled Structures* 151 (2020) 2–22.
- [15] L. Zhang, Y. Liang, O. Zhao, Experimental and numerical investigations of pin-ended hot-rolled stainless steel angle section columns failing by flexural buckling, *Thin-Walled Structures* 156 (2020) 1–11.
- [16] AISC Design Guide 27: Structural Stainless Steel, Am. Institute of Steel Construction, 2013.
- [17] Design Manual for Structural Stainless Steel, fourth ed., Steel Construction Institute (SCI) P413, 2017.
- [18] A. Filipović, J. Dobrić, N. Baddoo, P. Može, Experimental response of hot-rolled stainless steel angle columns, *Thin-Walled Structures*, 163 (2021) 107659.
- [19] A. Filipović, J. Dobrić, D. Buđevac, N. Fric, N. Baddoo, Experimental study of laser-welded stainless steel angle columns, *Thin-Walled Structures*, 164 (2021) 107777.
- [20] Montanstahl AG. (2020) <https://www.montanstahl.com/>
- [21] Eurocode 3: Design of steel structures – Part 1-1: General rules and rules for buildings EN 1993-1-1, CEN, Brussels (Belgium), 2005.
- [22] Specification for Structural Steel Buildings, An American National Standard ANSI/AISC 360-16 American Institute of Steel Construction (AISC), Chicago, 2016.
- [23] ABAQUS User Manual, Version 6.12, Providence, RI, USA: DS SIMULIA Corp; 2012.
- [24] J. Dobrić, A. Filipović, N. Baddoo, Z. Marković, D. Buđevac, Design procedures for cold-formed stainless steel equal-leg angle columns, *Thin-Walled Structures* 159, 107210, (2021).
- [25] EN 10025-2: Hot rolled products of structural steels - Part 2: Technical delivery conditions for non-alloy structural steels, CEN Brussels (Belgium), 2019.
- [26] EN 10025-3: Hot rolled products of structural steels - Part 3: Technical delivery conditions for normalized/normalized rolled weldable fine grain structural steels, CEN, Brussels (Belgium), 2019.

- [27] Manual on stability of steel structures. European Convention for Constructional Steelwork (ECCS), 1976.
- [28] S. Kitipornchai, H.W. Lee, Inelastic buckling of single-angle, tee and double-angle struts, *Journal of Constructional Steel Research* 6 (1986) 219-236.
- [29] D. Camotim, P.B. Dinis, A. Landesmann, Behavior, failure and Direct Strength Method design of steel angle columns: geometrical simplicity versus structural complexity, *Journal of Structural Engineering (ASCE)*, 146 (11) (2020).
- [30] P. Može, L. G. Cajot, F. Sinur, K. Rejec, D. Beg, Residual stress distribution of large steel equal leg angles, *Engineering Structures* 7 (2014) 35–47.
- [31] H. Ban, G. Shi, Y. Shi, Y. Wang, Residual Stress Tests of High-Strength Steel Equal Angles, *Journal of Structural Engineering* 138 (2012) 1446–1454.
- [32] Y. Huang, B. Young, Experimental investigation of cold-formed lean duplex stainless steel beam-columns, *Thin-Walled Structures*, 76 (2014) 105–117.
- [33] EN 10056-2: Structural steel equal and unequal leg angles – Part 2: Tolerances on shape and dimensions, CEN, Brussels (Belgium), 1998.
- [34] EN 1090-2: Execution of steel structures and aluminium structures – Part 2: Technical requirements for steel structures, CEN, Brussels (Belgium), 2008.
- [35] Eurocode 3: Design of steel structures – Part 1-5: Plated structural elements EN 1993-1-5, CEN, Belgium (Brussels), 2006.
- [36] K.J.R. Rasmussen, G.J. Hancock, Design of cold-formed stainless steel tubular members I: Columns, *J. Struct. Eng.*, ASCE 119 (8) (1993) 2349–2367.
- [37] L. Gardner, D. A. Nethercot, Numerical modeling of stainless steel structural components a consistent approach, *J. Struct. Eng.*, ASCE 130 (10) (2004) 1586–1601.
- [38] B. Behzadi-Sofiani, L. Gardner, M. A. Wadea, P. B. Dinis, D. Camotim, Behaviour and design of fixed-ended steel equal-leg angle section columns, *Journal of Constructional Steel Research*, 182 (2021) 106649.



- [39] P.B. Dinis, D. Camotim, N. Silvestre, On the mechanics of thin-walled angle column instability, *Thin-Walled Structures* 52 (2012) 80-89.
- [40] Eurocode: Basis of structural design EN 1990, European Committee for Standardization (CEN), Brussels (Belgium), 2002.
- [41] S. Afshan, P. Francis, N. R. Baddoo, L. Gardner, Reliability analysis of structural stainless steel design provisions, *Journal of Constructional Steel Research*, 114 (2015) 293–304.